

1 **ShellChron 0.4.0: A new tool for constructing chronologies in accretionary carbonate archives**
2 **from stable oxygen isotope profiles**

3 Niels J. de Winter^{1,2}

4 ¹Department of Earth Sciences, Utrecht University, Utrecht, the Netherlands

5 ²AMGC research group, Vrije Universiteit Brussel, Brussels, Belgium

6

7 Corresponding author: Niels J de Winter (n.j.dewinter@uu.nl)

8

9

10

11 **Abstract**

12 This work presents ShellChron, a new model for generating accurate internal age-models for high-
13 resolution paleoclimate archives, such as corals, mollusk shells and speleothems. Reliable sub-annual
14 age models form the backbone of high-resolution paleoclimate studies. In absence of independent sub-
15 annual growth markers in many of these archives, the most reliable method for determining the age of
16 samples is through age modelling based on stable oxygen isotope or other seasonally controlled proxy
17 records. ShellChron expands on previous solutions to the age model problem by fitting a combination
18 of a growth rate and temperature sinusoid to model seasonal variability in the proxy record in sliding
19 window approach. This new approach creates smoother, more precise age-distance relationships for
20 multi-annual proxy records with the added benefit of allowing assessment of the uncertainty on the
21 modelled age. The modular script of ShellChron allows the model to be tailored to specific archives,
22 without being limited to oxygen isotope proxy records or carbonate archives, with high flexibility in
23 assigning the relationship between the input proxy and the seasonal cycle. The performance of
24 ShellChron in terms of accuracy and computation time is tested on a set of virtual seasonality records
25 and real coral, bivalve and speleothem archives. The result shows that several key improvements in
26 comparison to previous age model routines enhance the accuracy of ShellChron on multi-annual records
27 while limiting its processing time. The current full working version of ShellChron enables the user to

28 model the age of a 10-year long high-resolution (16 samples/yr) carbonate records with monthly
29 accuracy within one hour of computation time on a personal computer. The model is freely accessible
30 on the CRAN database and GitHub. Members of the community are invited to contribute by adapting
31 the model code to suit their research topics.

32

33

34 **1. Introduction**

35 Fast growing carbonate archives, such as coral skeletons, mollusk shells and speleothems, contain a
36 wealth of information about past and present climate and environment (e.g. Urban et al., 2000; Wang et
37 al., 2001; Steuber et al., 2005; Butler et al., 2013). Recent advances in analytical techniques have
38 improved our ability to extract this information and obtain records of the conditions under which these
39 carbonates precipitated at high temporal resolutions, often beyond the annual scale (Treble et al., 2007;
40 Saenger et al., 2017; Vansteenberge et al., 2019; de Winter et al., 2020a). Key to the interpretation of
41 such records is the development of reliable chemical or physical proxies for climate and environmental
42 conditions which can be measured on a sufficiently fine scale to allow variability to be reconstructed at
43 the desired time resolution. Examples of suitable proxies include observations of variability in carbonate
44 fabric and microstructure and in (trace) elemental and isotopic composition (Frisia et al., 2000; Lough,
45 2010; Ullmann et al., 2010; Schöne et al., 2011; Ullmann et al., 2013; Van Rampelbergh et al., 2014; de
46 Winter et al., 2017). The unique preservation potential of carbonates in comparison with archives of
47 climate variability at similar time resolutions, such as tree ring records and ice cores, now allows us to
48 recover information about climate and environment of the geological past from these proxies on the
49 (sub-)seasonal scale (Ivany and Runnegar, 2010; Ullmann and Korte, 2015; Vansteenberge et al., 2016;
50 de Winter et al., 2018; 2020b; c; Mohr et al., 2020). The importance of this development cannot be
51 overstated because variability at high (daily and seasonal) resolution constitutes the most significant
52 component of climate variability (Mitchell, 1976; Huybers and Curry, 2006; Zhu et al., 2019). Accurate
53 reconstructions of this type of variability are therefore fundamental to our understanding of Earth's
54 climate system and critical for projecting its behavior in the future under anthropogenic global warming
55 conditions (IPCC, 2018).

56 A reliable age model is crucial to the interpretation of high-resolution carbonate records. An age model
57 is defined as a set of rules or markers that allows the translation of the location of a measurement or
58 observation on the archive to the time at which the carbonate was precipitated. This translation is
59 required for aligning records from multiple proxies or archives to a common time axis. Age alignment
60 enables data to be intercomparable and to be interpreted in the context of processes playing a role at
61 similar timescales. Age models are based on knowledge about the growth or accretion rate of the archive
62 through time. Many high-resolution carbonate archives contain growth markers on which age models
63 can be based (e.g. Jones, 1983; Le Tissier et al., 1994; Verheyden et al., 2006). These are especially
64 valuable in some mollusk species, in which growth lines demarcate annual, daily, or even tidal cycles
65 (e.g. *Arctica islandica*, Schöne et al., 2005; *Pecten maximus*, Chavaud et al., 2005 and *Cerastoderma*
66 *edule*, Mahé et al., 2010). However, in many mollusk species and most carbonate archives, such
67 independent growth indicators are absent or too infrequent to (relatively) date high-resolution
68 measurements (Judd et al., 2018; Huyghe et al., 2019). In such cases, age models need to be based
69 on alternative indicators.

70 The oxygen isotope composition of carbonates ($\delta^{18}\text{O}_c$) is closely dependent on the isotopic composition
71 of the fluid ($\delta^{18}\text{O}_w$) and the temperature at which the carbonate is precipitated (Urey, 1948; McCrea,
72 1950; Epstein et al., 1953). In most natural surface environments, either one or both factors is strongly
73 dependent on the seasonal cycle, one generally being dominant over the other. This causes carbonates
74 precipitated in these environments to display strong quasi-sinusoidal variations in $\delta^{18}\text{O}_c$ that follow the
75 seasonal cycle (e.g. Dunbar and Wellington, 1981; Jones and Quitmyer, 1996; Baldini et al., 2008).
76 Examples of this behavior include seasonal cyclicity in sea surface temperatures recorded in the $\delta^{18}\text{O}_c$
77 of corals and mollusks and seasonal cyclicity in the $\delta^{18}\text{O}_w$ of precipitation recorded in speleothems
78 (Dunbar and Wellington, 1981; Schöne et al., 2005; Van Rampelbergh et al., 2014). This relationship is
79 challenged in tropical latitudes, where temperature seasonality is restricted. However, in some tropical
80 archives, the annual cycle of $\delta^{18}\text{O}_w$ in precipitation still allows the annual cycle to be resolved from $\delta^{18}\text{O}$
81 records (e.g. Evans and Schrag, 2004). These properties make $\delta^{18}\text{O}_c$ one of the most highly sought-
82 after proxies for climate variability, and high-resolution $\delta^{18}\text{O}_c$ records are abundant in the paleoclimate
83 literature (e.g. Lachniet, 2009; Lough, 2010; Schöne and Gillikin, 2013 and references therein).

84 The close relationship between $\delta^{18}\text{O}_c$ records and the seasonal cycle can also be exploited to estimate
85 variability in growth rate of the archive. This property of $\delta^{18}\text{O}_c$ curves has been recognized by previous

86 authors, and attempts have been made to quantify intra-annual growth rates from the shape of $\delta^{18}\text{O}_c$
87 profiles (Wilkinson and Ivany, 2002; Goodwin et al., 2003; De Ridder et al., 2006; Goodwin et al., 2009;
88 De Brauwere et al., 2009; Müller et al., 2015; Judd et al., 2018). Over time, these so called “growth
89 models” have improved from fitting of sinusoids to $\delta^{18}\text{O}_c$ data (Wilkinson and Ivany, 2002; De Ridder et
90 al., 2006) to including increasingly complicated (inter)annual growth rate curves to the model to fit the
91 shape of the $\delta^{18}\text{O}_c$ data (Goodwin et al., 2003; 2009; Müller et al., 2015; Judd et al., 2018). These later
92 models manage to fit the shape of $\delta^{18}\text{O}_c$ records well, but they often rely on detailed *a priori* knowledge
93 of growth rate or temperature patterns (e.g. Goodwin et al., 2003; 2009), which requires measurements
94 of one or more parameters in the environment. These measurements are not available in studies on
95 carbonate archives from the archeological or geological past. In contrast, the latest model by Judd et al.
96 (2018) is based only on the assumption that growth and temperature follow quasi-sinusoidal patterns
97 and can therefore work with $\delta^{18}\text{O}_c$ data alone, making it more widely applicable. The simplified
98 parameterization of temperature and growth rate seasonality by Judd et al. (2018) using two (skewed)
99 sinusoids is demonstrated to approximate natural circumstances very well.

100 However, the approach by Judd et al. (2018) is still limited in its use, because it requires whole, individual
101 growth years to be analyzed separately, resulting in a discontinuous time series when applied on records
102 containing multiple years of $\delta^{18}\text{O}_c$ data and no solution for incomplete years. In addition, the model has
103 no option to supply information about the less dominant factor that drives $\delta^{18}\text{O}_c$ values ($\delta^{18}\text{O}_w$ of sea
104 water in the case of mollusks and corals). Furthermore, only estimates from aragonite records are
105 supported, while the other dominant carbonate mineral, calcite, has a different temperature relationship
106 (Kim and O’Neil, 1997). Finally, neither of the models highlighted above except for the MoGroFun model
107 by Goodwin et al. (2009) include any assessment of the uncertainty of the constructed age model.

108 Here, a new model for estimating ages of samples in seasonal $\delta^{18}\text{O}_c$ curves is presented which
109 combines the advantages of previous models while attempting to negate their disadvantages.
110 ShellChron combines a skewed growth rate sinusoid with a sinusoidal temperature curve to model $\delta^{18}\text{O}_c$
111 using the Shuffled Complex Evolution model developed at the University of Arizona (SCEUA; Duan et
112 al., 1992; following Judd et al., 2018). It applies this optimization using a sliding window through the
113 dataset (as in Wilkinson and Ivany, 2002) and includes the option to use a Monte Carlo simulation
114 approach to combine uncertainties on the input ($\delta^{18}\text{O}_c$ and sample distance measurements) and the
115 model routine (as in Goodwin et al., 2009). As a result, ShellChron produces a continuous time series

116 with a confidence envelope, supports records from multiple carbonate minerals and allows the user to
 117 provide information on the less dominant variable influencing $\delta^{18}\text{O}_c$ (e.g. $\delta^{18}\text{O}_w$) if available (see **section**
 118 **2**). The modular design of ShellChron's functional script allows parts of the model to be adapted and
 119 interchanged, supporting a wide range of climate and environmental archives. As a result, the initial
 120 design of ShellChron for reconstructing age models in temperature-dominated $\delta^{18}\text{O}_c$ records from
 121 marine bio-archives (e.g. corals and mollusks) presented here can be easily modified for application on
 122 other types of records. The routine is worked out into a ready-to-use package for the open-source
 123 computational programming language R and is directly available without restrictions, allowing all
 124 interested parties to freely modify and build on the base structure to adapt it to their needs (R Core
 125 Team, 2020; full package code and documentation in **SI1**, see also **Code availability**).

126

127 2. Scientific basis

128 The relationship between $\delta^{18}\text{O}_c$ and the temperature of carbonate precipitation was first established by
 129 Urey (1951) and later refined with additional measurements and theoretical models (Epstein et al., 1953;
 130 Tarutani et al., 1969; Grossman and Ku, 1986; Kim and O'Neil, 1997; Coplen, 2007; Watkins et al.,
 131 2014; Daëron et al., 2019). Empirical transfer functions for aragonite and calcite by Grossmann and Ku
 132 (1986; modified by Dettmann et al., 1999; **equation 1**) and Kim and O'Neil (1997; **equation 2**, with
 133 VSMOW to VPDB scale conversion following Brand et al., 2014; **equation 3**) have so far found most
 134 frequent use in modern paleoclimate studies and are therefore applied as default relationships in the
 135 ShellChron model (see *d18O_model* function).

$$136 \quad T[^\circ\text{C}] = 20.6 - 4.34 * (\delta^{18}\text{O}_c[\text{‰VPDB}] - \delta^{18}\text{O}_w[\text{‰VSMOW}] + 0.2) \quad (1)$$

$$137 \quad 1000 * \ln(\alpha) = 18.03 * \frac{10^3}{(T[^\circ\text{C}] + 273.15)} - 32.42$$

$$138 \quad \text{with } \alpha = \frac{\left(\frac{\delta^{18}\text{O}_c[\text{‰VPDB}]}{1000} + 1\right)}{\left(\frac{\delta^{18}\text{O}_w[\text{‰VPDB}]}{1000} + 1\right)} \quad (2)$$

$$139 \quad \delta^{18}\text{O}_w[\text{‰VPDB}] = 0.97002 * \delta^{18}\text{O}_w[\text{‰VSMOW}] - 29.98 \quad (3)$$

140 To apply these formulae, it is assumed that carbonate is precipitated in equilibrium with the precipitation
141 fluid. Which carbonates are precipitated in equilibrium has long been subject to debate, and the
142 development of new techniques for measuring the carbonate-water system (e.g. clumped and dual-
143 clumped isotope analyses; Daëron et al., 2019; Bajnai et al., 2020) has led recent authors to challenge
144 the assumption that equilibrium fractionation is the norm (see **Supplementary Discussion**). The
145 modular character of ShellChron allows the empirical transfer function to be adapted to the $\delta^{18}\text{O}_c$ record
146 or to the user's preference for alternative transfer functions by a small modification of the *d18O_model*
147 function. Future versions of the model will include more options for changing the transfer function (see
148 **Model description**).

149 As the name suggests, the ShellChron model was initially developed for application on $\delta^{18}\text{O}_c$ records
150 from marine calcifiers (e.g. mollusk shells and corals). ShellChron approximates the evolution of the
151 calcification temperature at which the carbonate is precipitated by a sinusoidal function (see **equation**
152 **4, Table 1** and **SI4**; *temperature_curve* function; visualized in **Fig. 4A** and **Fig S1**), a good approximation
153 of seasonal temperature fluctuations in most marine and terrestrial environments (Wilkinson and Ivany,
154 2002). Variability in $\delta^{18}\text{O}_w$ is also comparatively limited in most marine environments (except for regions
155 with sea ice formation), making the model easy to use in these settings (LeGrande and Schmidt, 2006;
156 Rohling, 2013). Nevertheless, ShellChron includes the option to provide *a priori* knowledge about $\delta^{18}\text{O}_w$,
157 ranging from annual average values to detailed seasonal variability, enabling the model to work in
158 environments with more complex interaction between $\delta^{18}\text{O}_w$ and temperature on the $\delta^{18}\text{O}_c$ record (see
159 **equations 1 and 2**). This $\delta^{18}\text{O}_w$ data can be provided either as a vector (with the same length as the
160 data) or a single value (assuming constant $\delta^{18}\text{O}_w$) through the *d18Ow* parameter in the *run_model*
161 function.

$$T[^\circ\text{C}] = T_{av} + \frac{T_{amp}}{2} \sin\left(\frac{2\pi * \left(t[d] - T_{pha} + \frac{T_{per}}{4}\right)}{T_{per}}\right) \quad (4)$$

163

Table 1: Overview of model parameters

Name	Description	Unit	Range
T_{av}	Average temperature	°C	Variable, generally between 0°C–30°C
T_{amp}	Temperature range (2*amplitude)	°C	Variable, generally <20°C
T_{pha}	Phase of temperature sinusoid	d	0–365 days
T_{per}	Period of temperature sinusoid	d	365 days by default
G_{av}	Average growth rate	µm/d	Variable, generally between 0–100 µm/day
G_{amp}	Range of growth rates	µm/d	Variable, generally <200 µm/day
G_{pha}	Phase of growth rate sinusoid	d	0–365 days
G_{per}	Period of growth rate sinusoid	d	365 days by default
G_{skw}	Skewness factor of GR sinusoid	-	0–100, with 50 meaning no skew
D	Distance along the record	µm	Depends on archive
t	Age	d	Depends on archive
L_{win}	Length of sampling window	#	Depends on sampling resolution
w	Weighing factor on sample	-	0–1
i	Position relative to model window	-	0– L_i
I	Intercept of sinusoid (T_{av} or G_{av})		
A	Amplitude of sinusoid $\left(\frac{T_{amp}}{2} \text{ or } \frac{G_{amp}}{2}\right)$		
P	Period of sinusoid (T_{per} or G_{per})	d	
φ	Phase of sinusoid (T_{pha} or G_{pha})	d	

164

165 If marine $\delta^{18}O_c$ records represent one extreme on the spectrum of temperature versus $\delta^{18}O_w$ influence
166 on the $\delta^{18}O_c$ record, cave environments, in which $\delta^{18}O_c$ variability is predominantly driven by $\delta^{18}O_w$
167 variability in the precipitation fluid, represent the other extreme (Van Rampelbergh et al., 2014). In its
168 current form, ShellChron takes $\delta^{18}O_w$ as a user-supplied parameter to model temperature and growth
169 rate variability, but future versions will allow temperature to be fixed, while $\delta^{18}O_w$ becomes the modelled
170 variable. ShellChron’s modular character makes it possible to implement this update without changing
171 the structure of the model. Application of ShellChron on $\delta^{18}O_c$ records from cave deposits will have to
172 be treated with caution, since drip water $\delta^{18}O_w$ seasonality (if present) cannot always be approximated
173 by a sinusoidal function and equilibrium fractionation in cave deposits is less common than in bio-
174 archives (Baldini et al., 2008; Daëron et al., 2011; Van Rampelbergh et al., 2014).

175 Besides temperature (or $\delta^{18}O_w$) seasonality, ShellChron models the growth rate of the archive to
176 approximate the $\delta^{18}O_c$ record (see **equation 5**, **Table 1** and **SI4**; *growth_rate_curve* function; visualized
177 in **Fig. 4B** and **Fig S2**). Since the growth rate in many carbonate archives varies seasonally, a quasi-
178 sinusoidal model for growth rate seems plausible (e.g. Le Tissier et al., 1994; Baldini et al., 2008; Judd
179 et al., 2018). However, as discussed in Judd et al. (2018), the occurrence of growth cessations (growth
180 rate = 0) and skewness in seasonal growth patterns calls for a more complex growth rate model that
181 can take these properties into account. Therefore, ShellChron uses a slightly modified version of the

182 skewed sinusoidal growth function described by Judd et al. (2018; **equation 5**). Note that the added
 183 complexity of this function does not preclude the modelling of growth rate functions described by a
 184 simple sinusoid (no skewness; $G_{skw} = 50$) or even constant growth through the year ($G_{amp} = 0$; see **Table**
 185 **1**).

$$186 \quad G[mm/yr] = G_{av} + \frac{G_{amp}}{2} \sin\left(\frac{2\pi * (t[d] - G_{pha} + G_{per} * S)}{P}\right)$$

$$187 \quad \text{with } S = \begin{cases} \frac{100 - G_{skw}}{50}, & \text{if } t[d] - G_{pha} < G_{per} \frac{100 - G_{skw}}{100} \\ \frac{G_{skw}}{50}, & \text{if } t[d] - G_{pha} \geq G_{per} \frac{100 - G_{skw}}{100} \end{cases} \quad (5)$$

188 Contrary to previous $\delta^{18}\text{O}_c$ growth models, ShellChron allows uncertainties on the input variables
 189 (sampling distance and $\delta^{18}\text{O}_c$ measurements) as well as uncertainties of the full modelling approach to
 190 be propagated, providing confidence envelopes around the chronology. Uncertainty propagation is
 191 optional and can be skipped without compromising model accuracy. Standard deviations of uncertainties
 192 on input variables (sampling distance and $\delta^{18}\text{O}_c$) can be provided by the user, while model uncertainties
 193 are calculated from the variability in model results of the same datapoint obtained from overlapping
 194 simulation windows (see *growth_model* function). Measurement errors are combined by projecting
 195 Monte Carlo simulated values for sampling distance and $\delta^{18}\text{O}_c$ measurements on the modelled $\delta^{18}\text{O}_c$
 196 curve through an orthogonal projection (**equation 6**; *mc_err_orth* function; visualized in **Fig S3**). The
 197 measurement uncertainty projected on the distance domain is then combined with the model uncertainty
 198 to obtain pooled uncertainties in the distance domain, which are propagated through the modelled $\delta^{18}\text{O}_c$
 199 record to obtain uncertainties on the model result in the age domain. As a result of the sliding window
 200 approach in ShellChron, model results for datapoints situated at the edges of windows are more
 201 sensitive to small changes in the modelled parameters and therefore possess a larger model
 202 uncertainty. To prevent these least certain model estimates from affecting the stability of the model,
 203 model results are given more weight the closer they are situated towards the center of the model window
 204 (see **equation 7** in *export_results* function; see also **Fig. S4**). This weighing is also incorporated in
 205 uncertainty propagation through a weighted standard deviation (see **equation 8** from the *sd_wt*
 206 function).

$$207 \quad \sigma_{meas} = \sqrt{\left(\frac{D_{sim} - \overline{D_{sim}}}{\sigma_D}\right)^2 + \left(\frac{\delta^{18}\text{O}_{sim} - \overline{\delta^{18}\text{O}_{sim}}}{\sigma_{\delta^{18}\text{O}}}\right)^2} \quad (6)$$

208

$$w[i] = 1 - \left| \frac{2i}{L_{window}} - 1 \right| \quad (7)$$

209

$$\sigma_{weighted,i} = \sqrt{\frac{w_i * (x_i - \bar{w})^2}{\sum w[i] * \frac{N-1}{N}}} \quad (8)$$

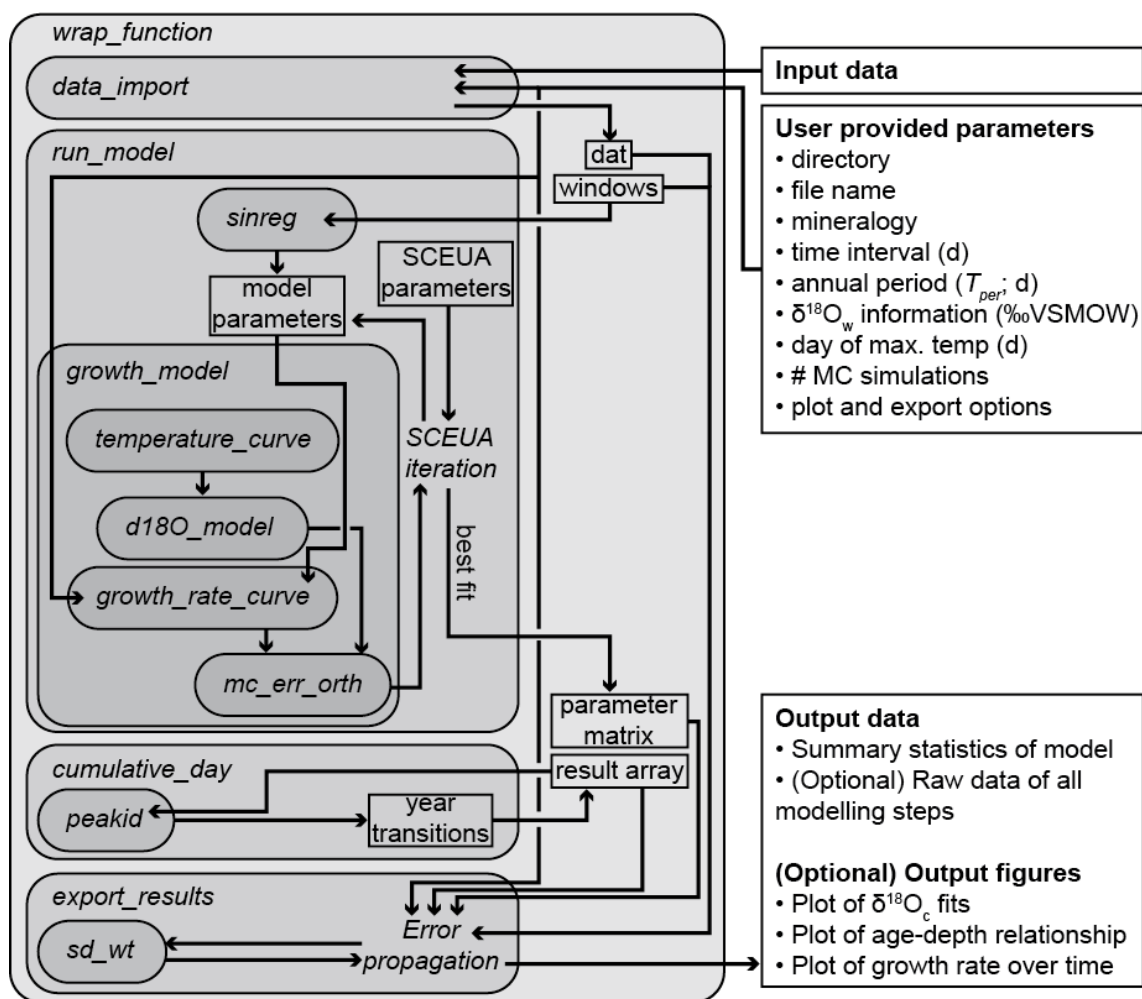
210

211 3. Model description

212 ShellChron is organized in a series of functions that describe the step-by-step modelling process. A
213 schematic overview of the model is given in **Fig. 1**. A short **Test Case** is used to illustrate the modelling
214 steps in ShellChron. **Fig. 2** shows how the virtual **Test Case** was created from randomly generated
215 seasonal growth rate, $\delta^{18}\text{O}_w$ and temperature curves using the *seasonalclumped* R package (de Winter
216 et al., 2021; see **Fig. 2, Supplementary Methods** and **S12**) A wrapper function (*wrap_function*) is
217 included which carries out all steps of the model procedure in succession to promote ease of use.

218

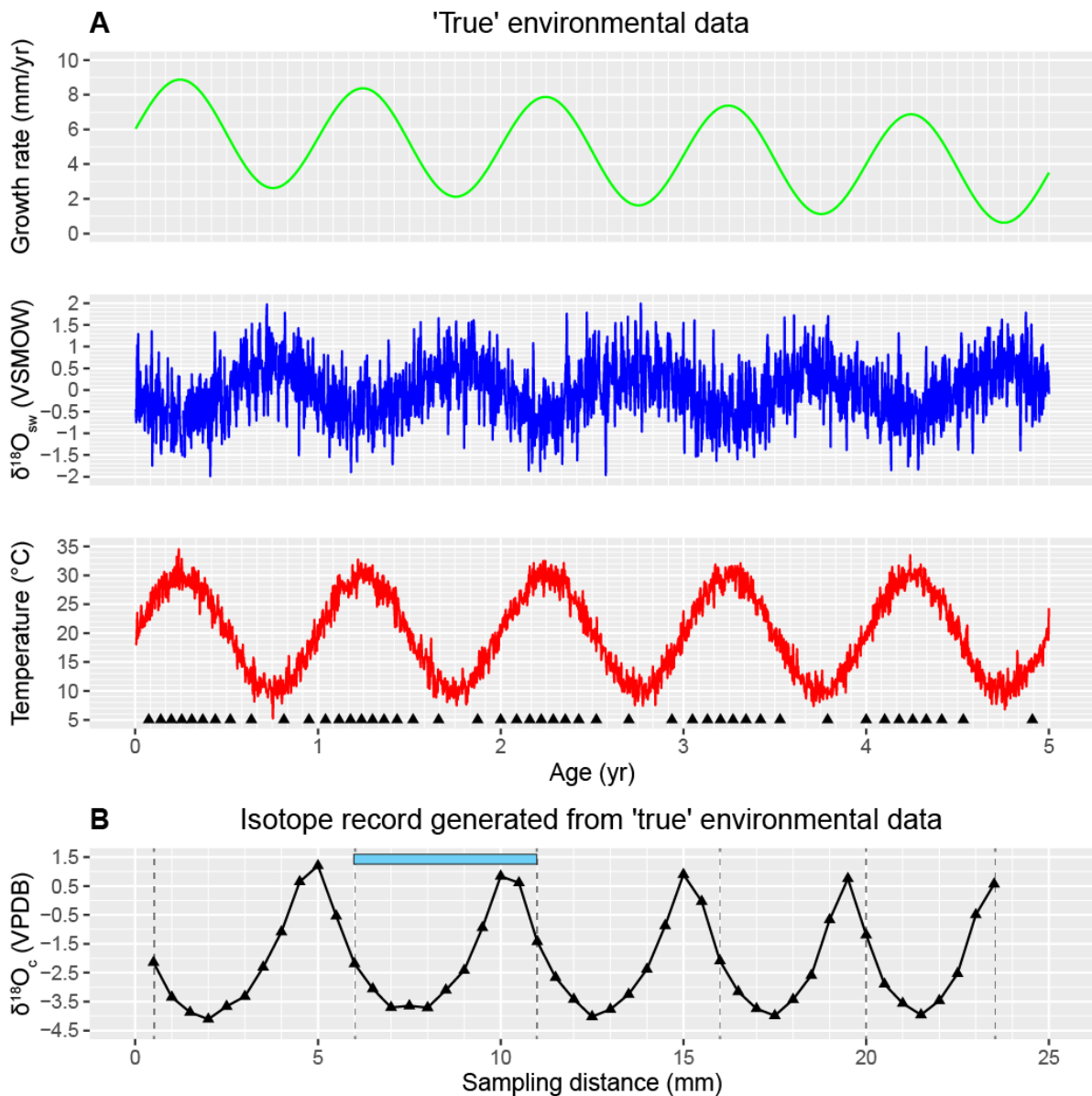
Schematic overview of ShellChron model



219

220 **Figure 1:** Schematic overview of ShellChron. Names in *italics* refer to functions (encapsulated in
 221 rounded rectangular boxes) and operations within functions. Rectangular boxes represent data. Arrows
 222 represent the flow of information between model components. Note that some operations are
 223 encapsulated in functions (e.g. *Error propagation* in *export results*) and that some functions are only
 224 used within other functions (e.g. *peakid* in *cumulative_day*). All data structures outside *wrap_function*
 225 represent input and output of the model. Detailed documentation of all functions and operations in
 226 ShellChron is provided in **SI1** (see also **Code availability**).

227



228

229 **Figure 2: A)** Plots of the growth rate (light green), $\delta^{18}\text{O}_{\text{w}}$ (blue) and Temperature (red) records (in time

230 domain) from which the **Test case** was produced. Black triangles on the bottom of the temperature

231 plot indicate the ages of the samples taken from the record. **B)** The $\delta^{18}\text{O}_{\text{c}}$ record for the **Test Case**

232 generated after equidistant sampling using the *seasonalclumped* package (de Winter et al., 2021) with

233 a sampling interval of 0.5 mm. Error bars on sampling distance (0.1 mm) and $\delta^{18}\text{O}_{\text{c}}$ (0.1‰) fall within

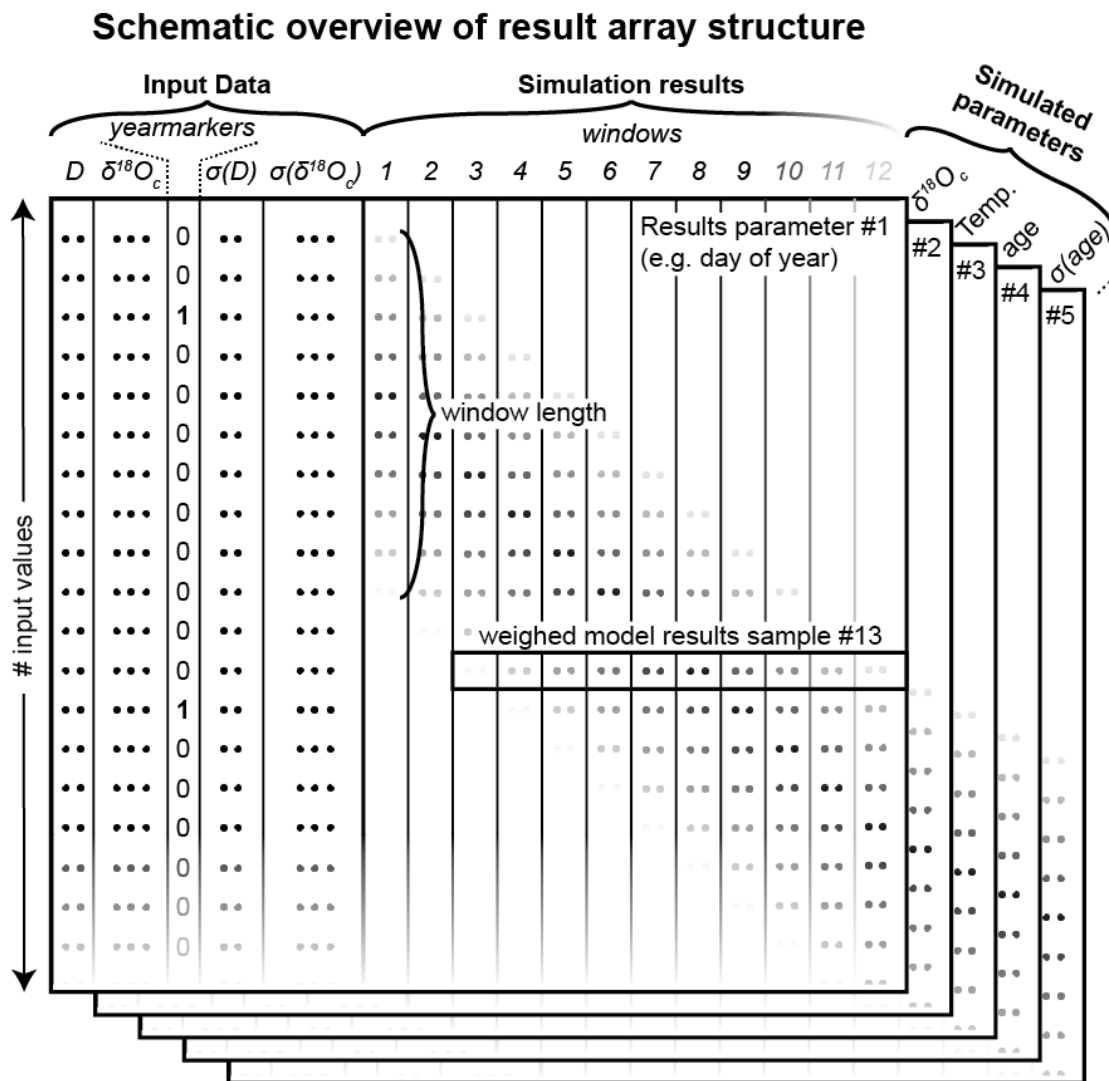
234 the symbols. Vertical grey dashed lines indicate user-provided year markers and the blue bar on top of

235 this plot shows an example of the width of a modelling window. See **Supplementary Methods** for

236 details on producing the **Test case** $\delta^{18}\text{O}_{\text{c}}$ record and **SI3** for the R script used to generate the data.

237 Data is imported through the *data_import* function, which takes a comma-separated text file (CSV) with
238 the input data. Data files need to contain columns containing sampling distance (D , in μm) and $\delta^{18}\text{O}_c$
239 data (in ‰VPDB), a column marking years in the record (*yearmarkers*) and two optional columns
240 containing uncertainties on sampling distance ($\sigma(D)$, one standard deviation, in μm) and $\delta^{18}\text{O}_c$ ($\sigma(\delta^{18}\text{O}_c)$,
241 one standard deviation, in ‰) respectively (see example in **SI2** and **Figure 3**). The function uses the
242 year markers (third column) as guidelines for defining the minimum length of the model windows to
243 ensure that all windows contain at least one year of growth. Window sizes are defined to contain at least
244 two year markers (see **Fig. 2**). By default, consecutive windows are shifted by one datapoint, yielding a
245 total number of windows equal to the sample size minus the length of the last window. While year
246 markers are required for ShellChron to run (otherwise no windows can be defined), the result of the
247 model does not otherwise depend on user-provided year markers, instead basing the age result purely
248 on simulations of the $\delta^{18}\text{O}_c$ data.

249



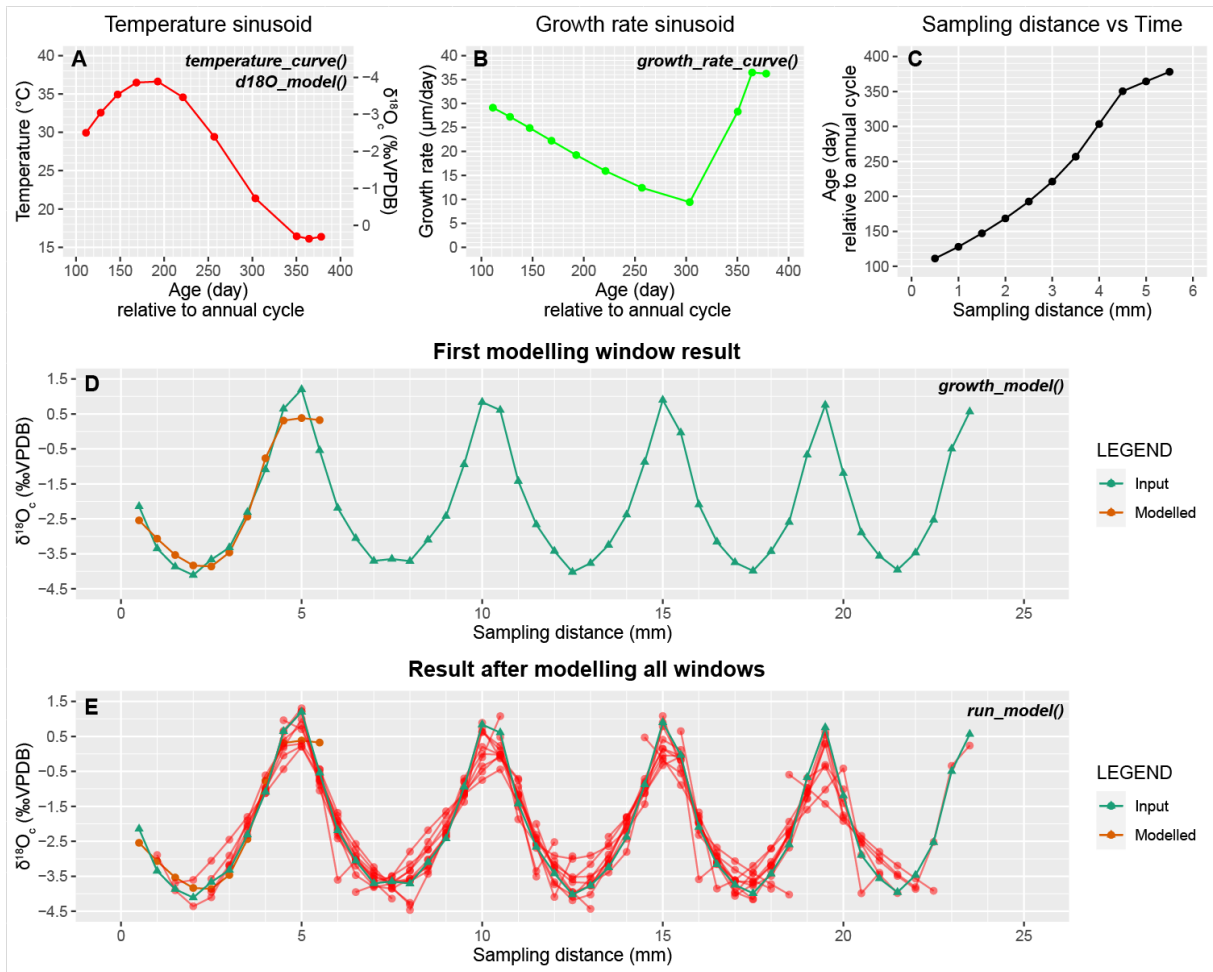
250

251 **Figure 3:** Schematic overview of the structure of the result array in which ShellChron stores the raw
 252 results of each model window. Data is stored in three dimensions: The sample number (rows in the
 253 figure), the window number (columns in the figure) and the number of modelled parameters
 254 (represented by the stacked table “sheets” in the figure). Note that the first 5 columns of each “sheet”
 255 represent the user-provided input data (see example in **SI2**), and that the model result data starts from
 256 column 6. The window length is determined by the user-provided indication of year transitions (column
 257 3). Rows of dots in the figure are placeholders for (input or result) values. Shading of these dots in the
 258 window columns indicate differential weighing of modelled values in function of their location relative to
 259 the sliding window. The horizontal box shows how these weighing factors within each sample window
 260 (in vertical direction) result in weighing of different estimates of modelled parameters for the same data
 261 point (in horizontal direction). Shading of input data and window number towards the bottom and right
 262 edge of the figure, respectively, indicates that the number of input values (and thus simulation

263 windows) is only limited to the length of the input table and may therefore continue indefinitely (at the
264 expense of longer computation times, see **Fig. 8** in **Model performance**).

265 The core of the model consists of simulations of overlapping subsamples (windows) of the sampling
266 distance and $\delta^{18}\text{O}_c$ data described by the *run_model* function (see **Fig. 1 and 3**). Data and window sizes
267 are passed from *data_import* onto *run_model* along with user-provided parameters (e.g. $\delta^{18}\text{O}_w$
268 information; see **Fig. 1**). *run_model* loops through the data windows and calls the *growth_model*
269 function, which fits a modelled $\delta^{18}\text{O}_c$ vs. distance curve through the data using the SCEUA optimization
270 algorithm (see Duan et al., 1992; see example in **Fig 4**). The simulated $\delta^{18}\text{O}_c$ curve is produced through
271 a combination of a temperature sinusoid (*temperature_curve* function; see **equation 4, Fig. 4A and Fig.**
272 **S1**) and a skewed growth rate sinusoid (*growth_rate_curve*; see **equation 5, Fig. 4B and Fig. S2**), with
273 temperature data converted to $\delta^{18}\text{O}_c$ data through the *d18O_model* function (**equation 1 and 2; Fig.**
274 **4A**).

275



276

277 **Figure 4:** Showing the steps taken to simulate $\delta^{18}\text{O}_c$ data in the *run_model()* function on the **Test case**.

278 **A)** Temperature sinusoid used to approximate $\delta^{18}\text{O}_c$ data in the first modelling window (see **D**), produced
 279 using a combination of *temperature_curve* and *d18O_model* functions. Symbols indicate the positions
 280 of $\delta^{18}\text{O}_c$ samples on the temperature curve, with estimated $\delta^{18}\text{O}_c$ values shown on the secondary axis
 281 (right). **B)** Skewed growth rate sinusoid fit to the $\delta^{18}\text{O}_c$ data using the *growth_rate_curve* function. Note
 282 the shift towards steeper growth rate increase around the 300th model day (autumn season in this
 283 example). See **Fig. S2** for a detailed description of the growth rate sinusoid. **C)** The modelled age-
 284 distance relationship for this window after fitting $\delta^{18}\text{O}_c$ data, resulting from aligning the estimated age of
 285 samples (x-axes on **A**) with the distance in sampling direction (x-axis in **D**) using the cumulative growth
 286 rate function (**B**). **D)** $\delta^{18}\text{O}_c$ profile of the **Test case** (green) with the $\delta^{18}\text{O}_c$ curve of the first modelling
 287 window (red), which results from the combination of temperature (**A**) and growth rate (**B**) sinusoids,
 288 plotted on top (*growth_model* function). **E)** Result after simulating the full $\delta^{18}\text{O}_c$ profile of the **Test case**
 289 (green) using *run_model*, with the $\delta^{18}\text{O}_c$ curves of individual modelling windows shown in red.

290 By default, starting values for the parameters describing temperature and growth rate curves are
 291 obtained by estimating the annual period (P) through a spectral density estimation and applying a
 292 linearized sinusoidal regression through the $\delta^{18}\text{O}_c$ data (*sinreg* function; see **equation 9**). It is possible
 293 to skip this sinusoidal modelling step through the “*sinfit*” parameter in the *run_model* function, in which
 294 case the starting value for the annual period is set equal to the width of the model window. In addition,
 295 *growth_model* takes a series of parameters describing the method for SCEUA optimization (see Duan
 296 et al., 1992; Judd et al., 2018) and the upper and lower bounds for parameters describing temperature
 297 and growth rate curves (see **SI4**). Parameters for the SCEUA algorithm (*iniflg*, *ngs*, *maxn*, *kstop*, *pcento*
 298 and *peps*) in the *run_model* function may be modified by the user to reach more desirable optimization
 299 outcomes. The effect of changing the SCEUA parameters on the model result for the **Test case** is
 300 illustrated in **section 4.1** (see **Fig. 5**). If uncertainties on sampling distance and $\delta^{18}\text{O}_c$ data are provided,
 301 *growth_model* calls the *mc_err_orth* function to propagate these errors through the model result (see
 302 **equation 6** and **Fig S3**).

$$303 \quad \delta^{18}\text{O}_c[\text{‰VPDB}] = I + \frac{A}{2} \sin\left(\frac{2\pi * \left(D - \varphi + \frac{P}{4}\right)}{P}\right),$$

$$304 \quad \text{linearized as: } \delta^{18}\text{O}_c[\text{‰VPDB}] = a + b \sin\left(\frac{2\pi}{P} * D\right) + c \cos\left(\frac{2\pi}{P} * D\right),$$

$$305 \quad \text{with } I = a; A = \sqrt{b^2 + c^2} \text{ and } \varphi = P * \left(0.25 - \frac{\cos^{-1}\left(\frac{b}{A}\right)}{2\pi}\right) \text{ (9)}$$

306 The *run_model* function returns an array listing day of the year (1–365), temperature, $\delta^{18}\text{O}_c$, growth rate
 307 and (optionally) their uncertainty standard deviations as propagated from uncertainties on the input data
 308 (“result array”; see **Fig. 3** and **SI5**). Note that the default length of the year (*Tper* and *Gper*) is set at 365
 309 days, but that these parameters can be modified by the user in *run_model*. In addition, a matrix
 310 containing the optimized parameters of temperature and growth rate curves is provided, yielding
 311 information about the evolution of mean values, phases, amplitudes, and skewness of seasonality in
 312 temperature and growth rate along the record (“parameter matrix”, see **Fig. 1** and **SI6**). To construct an
 313 age model for the entire record, the modelled timing of growth data, expressed as day relative to the
 314 365-day year, is converted into a cumulative time series listing the number of days relative to the start
 315 of the first year represented in the record (rather than relative to the start of the year in which the

316 datapoint is found). This requires year transitions (transitions from day 365 to day 1) to be recognized
317 in all the model results. The *cumulative_day* function achieves this by aggregating information about
318 places where the beginning and end of the year is recorded in individual window simulations and
319 applying a peak identification algorithm (*peakid* function) to find places in the record where year
320 transitions occur (see **Supplementary Methods**). Results of the timing of growth for each sample (in
321 day of the year) are converted to a cumulative time scale using their positions relative to these
322 recognized year transitions (**Supplementary Methods**).

323 In a final step (described by the *export_results* function), the results from overlapping individual
324 modelling windows are combined to obtain mean values and 95% confidence envelopes of the result
325 variables (age, $\delta^{18}\text{O}_c$, $\delta^{18}\text{O}_c$ -based temperatures and growth rates) for each sample in the input data. If
326 uncertainties on the input variables were provided, these are combined with uncertainties on the
327 modelling result calculated from results of the same datapoint on overlapping data windows by pooling
328 the variance of the uncertainties (**equation 10**). Throughout this merging of data from overlapping
329 windows, results from datapoints on the edge of windows are given less weight than those from
330 datapoints near the center of a window (see **equation 7** and **Fig. S4**). This weighing procedure corrects
331 for the fact that datapoints near the edge of a window are more susceptible to small changes in the
332 model parameters and are therefore less reliable than results in the center of the window. Finally,
333 summaries of the simulation results and the model parameters including their confidence intervals are
334 exported as comma-separated (CSV) files. In addition, *export_results* supports optional exports of
335 figures displaying the model results and files containing raw data of all individual model windows
336 (equivalent to “sheets” of the result array, see **Fig. 3** and **SI5**).

337
$$VAR_{pooled} = \frac{\sum_i((N_i-1)*VAR_i*w_i)}{\sum_i(N_i)-n} \quad (10)$$

338 in which w = weight of the individual reconstructions, N is the sample size and n is the number of
339 reconstructions (indexed by i) that is combined

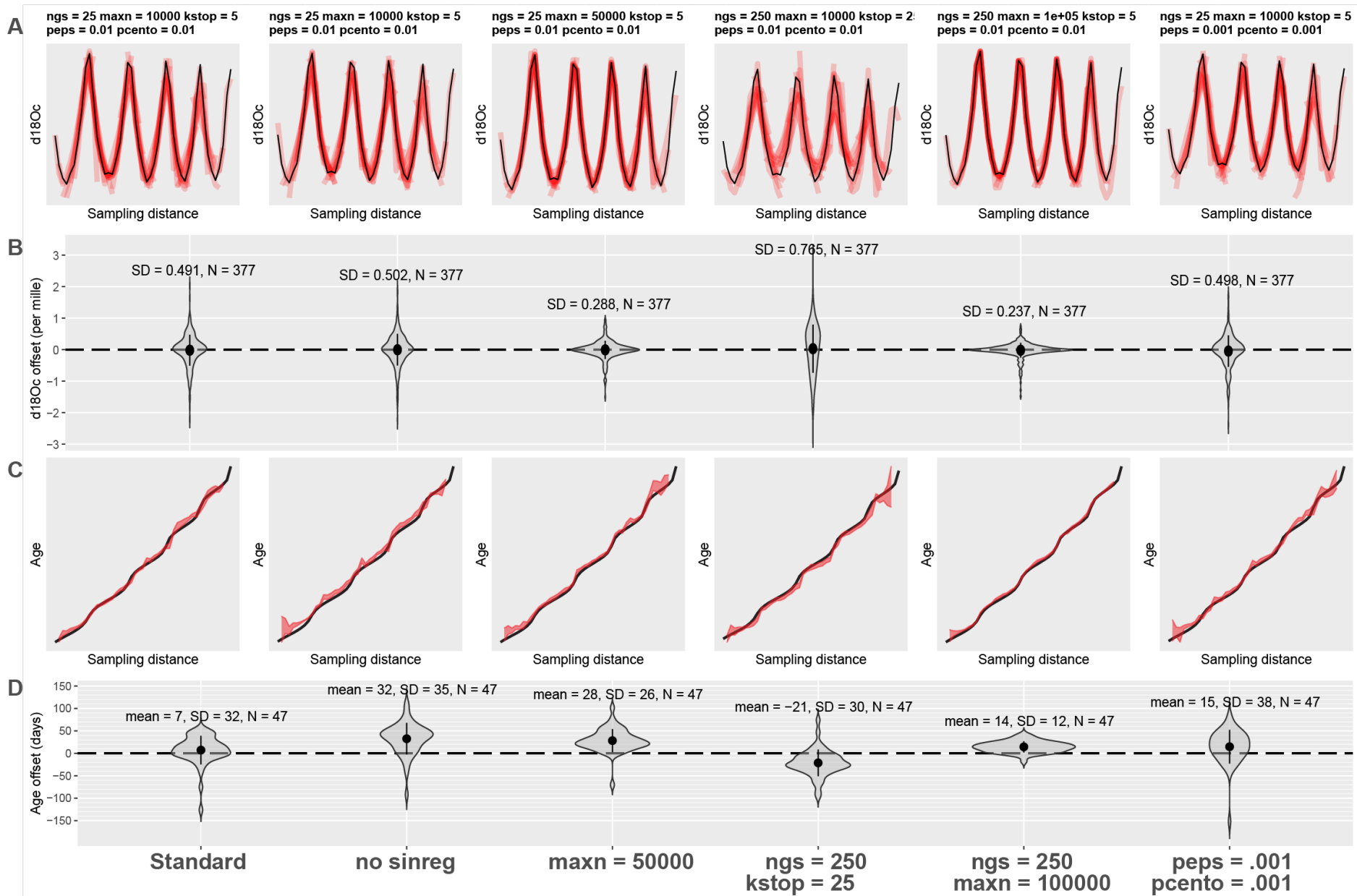
340

341 4. Model performance

342 The performance of ShellChron was first tested on three virtual datasets:

- 343 1. The short **Test case** used to illustrate the model steps above (see **Fig. 2** and **4**; **SI7**)
- 344 2. A $\delta^{18}\text{O}_c$ record constructed from a simulated temperature sinusoid with added stochastic noise
345 (**Case 1**; **SI8**)
- 346 3. A record based on a real high-resolution sea surface temperature and salinity record measured
347 on the coast of Texel island in the tidal basin of the Wadden Sea (North Netherlands; **Texel**,
348 see details in **SI9** and de Winter et al., 2021 and **Supplementary Methods**).

349 Firstly, the effect of varying parameters in the SCEUA algorithm is tested on the **Test Case** (**Fig. 5**).
350 Then, full model runs on **Case 1** and **Texel** are evaluated in terms of model performance (**Fig. 6**).
351 In addition to the three test cases, three modern carbonate $\delta^{18}\text{O}_c$ records were internally dated using
352 ShellChron (see **Fig. 7**): a tropical stony coral (*Porites lutea*; hereafter: **coral**) from the Pandora
353 Reef (Great barrier Reef, NE Australia; Gagan et al., 1993; see **SI10**), a Pacific oyster shell
354 (*Crassostrea gigas*; hereafter: **oyster**) from List Basin in Denmark (Ullmann et al., 2010; see **SI10**)
355 and a temperate zone speleothem from Han-sur-Lesse cave (Belgium; hereafter: **speleothem**; see
356 Vansteenberge et al., 2019; see **SI10**). Finally, ShellChron's performance in terms of computation
357 time and accuracy is compared to that of the most comprehensive pre-existing $\delta^{18}\text{O}_c$ -based age
358 model (by Judd et al., 2018) on simulated temperature sinusoids of various length and sampling
359 resolutions to which stochastic noise was added (*sensu* **Case 1**; de Winter et al., 2021; see **Fig. 8**
360 and **SI11**). The latter also demonstrates the scalability of ShellChron and its application on a variety
361 of datasets. Timing comparisons were carried out using a modern laptop (Dell XPS13–7390; Dell
362 Inc., Round Rock, Tx, USA) with an Intel Core i7 processor (8 MB cache, 4.1 GHz clock speed, 4
363 cores, Intel Corporation, Santa Clara, CA, USA), 16 GB LPDDR3 RAM and a SSD drive running
364 Windows 10. Note that ShellChron was built and tested successfully on Mac OS, Fedora Linux and
365 Ubuntu Linux as well.



367 **Figure 5:** Result of testing ShellChron with various combinations of SCEUA parameters and
368 sinusoidal regression on the **Test case** dataset (see **Fig. 2**). The leftmost plots illustrate performance
369 of ShellChron under default SCEUA parameters. Plots to the right show various combinations of
370 parameters that deviate from the default (see labels on top and bottom of plot) **A)** Fits of the model
371 $\delta^{18}\text{O}_c$ curves (red) with the data (black). **B)** Violin plots showing the distribution of modelled $\delta^{18}\text{O}_c$
372 offset from the data. **C)** Age-distance plots showing modelled (red) and true (black) age-depth
373 relationships for each scenario. **D)** Violin plots showing the distribution of age offsets from the real
374 age-depth relationship. SD = standard deviation, N = number of datapoints, sinres = sinusoidal
375 regression, maxn, ngs, kstop, peps and pcento are SCEUA parameters (see Duan et al., 1992 and
376 explanation in **section 4.1**). Data on test results is provided in **SI11**.

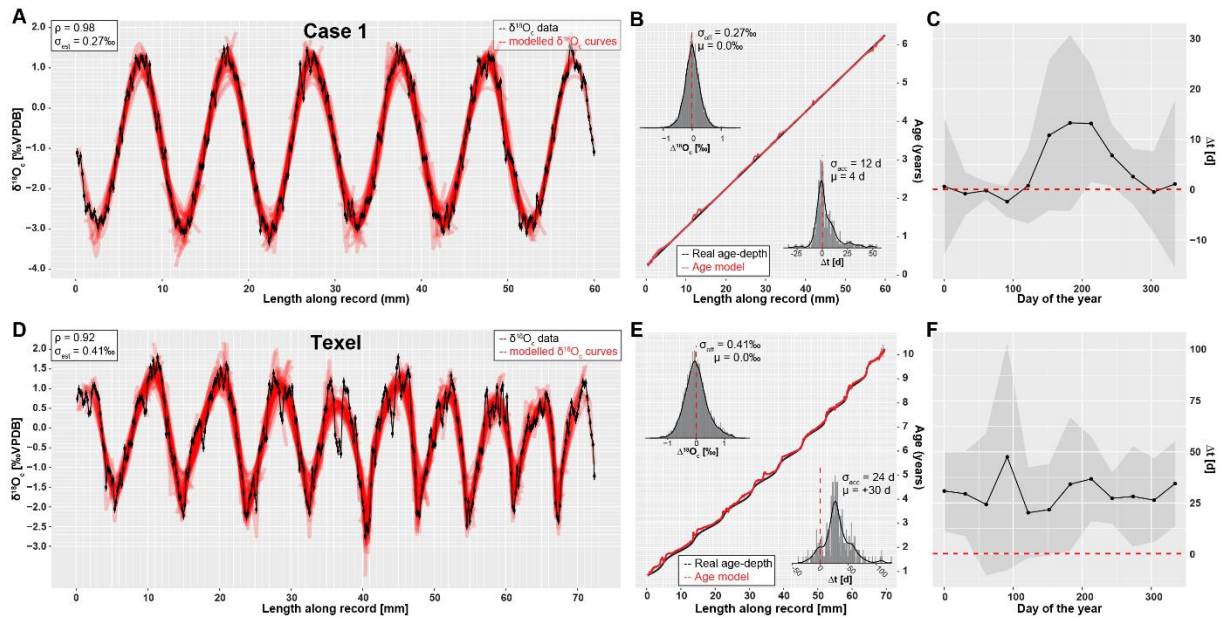
377 **4.1 Testing model parameters**

378 Testing different combinations of modelling parameters (**Fig. 5**) shows that, while the results of
379 ShellChron can improve beyond the default SCEUA parameters and sinusoidal regression, care must
380 be taken to evaluate the effect of changing modelling parameters on both the $\delta^{18}\text{O}_c$ fit and the age-
381 distance relationship. Comparative testing on the **Test case (Fig. 5)** shows that sinusoidal regression
382 has a negligible influence on the success of ShellChron fitting the $\delta^{18}\text{O}_c$ curve (**Fig. 5A-B**; standard
383 deviation on $\delta^{18}\text{O}_c$ is 0.49‰ with sinusoidal regression and 0.50‰ without). However, ShellChron with
384 sinusoidal regression performs better in terms of age approximation, with a mean age offset of only 7
385 \pm 32 days with sinusoidal regression against 32 \pm 35 days without (**Fig. 5C-D**). Age-distance plots
386 (**Fig. 5C**) show that the model without sinusoidal fit shows a phase offset with respect to the real age-
387 depth relationship, resulting in overestimation of the age for much of the record. Sinusoidal regression
388 probably results in better initial parameter estimation, which helps to avoid phase offsets like the one
389 shown in **Fig. 5**. For the remainder of the tests, sinusoidal regression was used.

390 The remainder of the tests show that the main bottleneck towards better $\delta^{18}\text{O}_c$ fit optimization is the
391 maximum number of function evaluations allowed within a single modelling cycle (maxn; see **Fig. 5**).
392 Increasing the other SCEUA parameters, such as the number of complexes in the SCEUA routine
393 (ngs), the number of shuffling loops that should show a significant change before convergence (kstop)
394 and the thresholds for significant change in parameter value (peps) or result value (pcento) does not
395 improve the result if the SCEUA algorithm is not allowed more processing time (maxn). In fact, **Fig. 5**

396 shows that increasing these SCEUA parameters can actually result in a worse $\delta^{18}\text{O}_c$ fit and higher
397 uncertainty on the age result (**Fig. 5B and D**). A fivefold increase in maxn (maxn = 50000) almost
398 halves the standard deviation on $\delta^{18}\text{O}_c$ residuals (from 0.49‰ to 0.29‰; **Fig. 5B**) and decreases the
399 standard deviation on the age model offset from 32 to 26 days (**Fig. 5D**). A combination of a tenfold
400 increase in function evaluations with an equal multiplication of the number of complexes in the SCEUA
401 routine (ngs; see details in Duan et al., 1992) results in a further reduction of standard deviations on
402 $\delta^{18}\text{O}_c$ (0.23‰) and age result (12 days). These tests show that returns in terms of model precision
403 quickly diminish with increasing processing time. Since the total modelling time linearly scales with the
404 number of function evaluations, this tradeoff towards lower standard deviation on the modelling result
405 is costly. Since these function evaluations are repeated in each modelling window, the cost in terms of
406 extra processing time can increase quickly, especially for larger $\delta^{18}\text{O}_c$ datasets. In addition, in this
407 situation the mean model offset (accuracy of the model; 7 days, 28 days and 14 days for maxn of $1.0 \cdot 10^4$,
408 $5.0 \cdot 10^4$ and $1.0 \cdot 10^5$ respectively; **Fig. 5D**) does not significantly improve with increasing number
409 of function evaluations. Based on these results, the default maxn parameter in ShellChron was set to
410 10^4 to compromise between keeping modelling times short while retaining high model accuracy.
411 However, specific datasets may benefit from an increase in modeling time, so case-by-case
412 assessment of the optimal SCEUA parameters is recommended. A detailed evaluation of the total
413 modelling time in a typical $\delta^{18}\text{O}_c$ dataset is discussed in **section 4.4**.

414



415

416 **Figure 6:** Result of applying ShellChron on two virtual datasets: **Case 1** (top, see **SI8**) and **Texel**,
 417 (bottom, see **SI9**). Leftmost panels (**A** and **D**) show the model fit of individual sample windows (red) on
 418 the data (black, including horizontal and vertical error bars), with in the top left Spearman's correlation
 419 coefficients (ρ) and standard deviations on the $\delta^{18}\text{O}_c$ estimate (σ_{est}). Middle panels (**B** and **E**) show the
 420 resulting age model (red, including shaded 95% confidence level) compared with the real age-distance
 421 relationship of both records. Histograms in the top left of age-distance plots show the offset between
 422 modelled and measured $\delta^{18}\text{O}_c$ (as visualized in panels **A** and **D**) with standard deviations of the $\delta^{18}\text{O}_c$
 423 offset (σ_{off}) and offset averages (μ). Histograms in the bottom right of age-distance plots show the offset
 424 between modelled and actual ages (in days) of each datapoint, including standard deviations on the age
 425 accuracy (σ_{acc}) and mean age offset (μ). Rightmost panels (**C** and **F**) highlight age offset binned in
 426 monthly time bins to illustrate how accuracy varies over the seasons. Grey envelopes indicate 95%
 427 confidence levels on the monthly age offset.

428

429 4.2 Artificial carbonate records

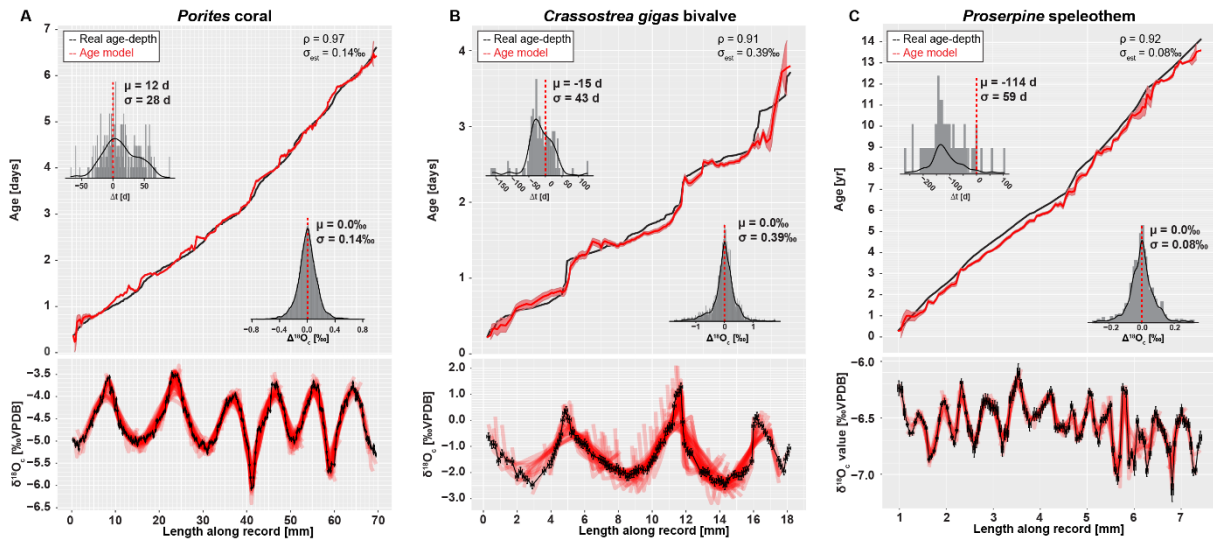
430 Results of running ShellChron on **Case 1** and **Texel** datasets (**Fig. 6**) show that modelled $\delta^{18}\text{O}_c$ records
431 in individual windows closely match the data. A summary of ShellChron performance statistics is given
432 in **Table 2**. In all virtual datasets, $\delta^{18}\text{O}_c$ estimates are equally distributed above and below the $\delta^{18}\text{O}_c$ data
433 ($\overline{\Delta^{18}\text{O}_c} = 0.0 \text{ ‰}$; Spearman's ρ of 0.98 and 0.92 for **Case 1** and **Texel** datasets respectively). Age
434 offsets vary slightly over the seasons, but the difference between monthly time bins is not statistically
435 significant on a 95% confidence level (**Fig. 6C** and **F**; see also **SI12**). The fact that seasonal bias in age
436 offset is absent in the **Texel** dataset, which is skewed towards growth in the winter season and includes
437 relatively strong seasonal variability in $\delta^{18}\text{O}_w$, shows that ShellChron is not sensitive to such subtle
438 (though common) variability in growth rate or $\delta^{18}\text{O}_w$. In general, ShellChron's mean age assignment is
439 accurate on a monthly scale (age offsets of $4 \pm 12 \text{ d}$ and $+30 \pm 24 \text{ d}$ for **Case 1** and **Texel** datasets
440 respectively). The sampling resolution in the **Texel** data decreases near the end of the record (see **SI9**),
441 but this does not result in reduced age model accuracy. If anything, the age of **Texel** samples is better
442 approximated near the end of the record, and age offsets are larger in the central part of the record
443 (~30-50 mm; **Fig. 6E**). The lower accuracy in the third to fifth year of the **Texel** record is likely a result
444 of the sub-annual variability in the record that is superimposed on the seasonal cycle. This variability is
445 less pronounced near the end of the record, partly because this variability is not resolved at lower
446 sampling resolution, which illustrates that higher sampling resolutions do not necessarily result in better
447 age models.

448

Table 2: Overview of datasets and model results

Dataset	Resolution	Length	$\delta^{18}\text{O}_c$ seasonal range	Complications
Test case	7-12 yr ⁻¹	5 yr	~5‰	Variable $\delta^{18}\text{O}_w$, Variable GR
Case 1	50 yr ⁻¹	6 yr	~4.3‰	None
Texel	26–45 yr ⁻¹	10 yr	~4‰	Variable $\delta^{18}\text{O}_w$, Variable GR
Coral	30–49 yr ⁻¹	6 yr	~1.7‰	Variable GR
Oyster	23–45 yr ⁻¹	3.5 yr	~3‰	Variable $\delta^{18}\text{O}_w$, Variable GR
Speleothem	4–13 yr ⁻¹	14 yr	~0.5‰	Variable $\delta^{18}\text{O}_w$, Variable GR, Non-sinusoidal $\delta^{18}\text{O}_c$ -forcing

Dataset	$\delta^{18}\text{O}_c$ offset ($\pm 1\sigma$)	Age offset ($\pm 1\sigma$)	Spearman's ρ	Observations
Test case	0.0 \pm 0.49 ‰	7 \pm 32 d	0.94	Slightly out of phase
Case 1	0.0 \pm 0.27‰	4 \pm 12 d	0.98	-
Texel	0.0 \pm 0.41‰	30 \pm 24 d	0.92	-
Coral	0.0 \pm 0.14‰	12 \pm 28 d	0.97	-
Oyster	0.0 \pm 0.39‰	-15 \pm 43 d	0.91	Reduced accuracy near growth stops
Speleothem	0.0 \pm 0.08‰	-114 \pm 59 d	0.92	Susceptible to phase offsets; Only reliable on inter-annual scale



450

451 **Figure 7:** Overview of model results for the three test datasets from real carbonate archives: **(A) coral**,
 452 **(B) oyster** and **(C) speleothem**. Lower panels indicate the fit of individual model windows (in red) with
 453 the data (in black) while upper panels show the age model (in red) compared to the “true” age-distance
 454 relationship with histograms showing model accuracy (in days, top left) and model fit ($\delta^{18}\text{O}_e$ offset in ‰,
 455 bottom right). Color scheme follows **Figure 3**. Note that the true age-distance relationship is not known
 456 for these natural records, but is estimated using known growth seasonality (**coral**), comparison with *in*
 457 *situ* temperature and salinity measurements (**oyster**) or simply by interpolating between annual growth
 458 lines (**speleothem**). See **Supplementary Methods** for details and **S110** for raw data.

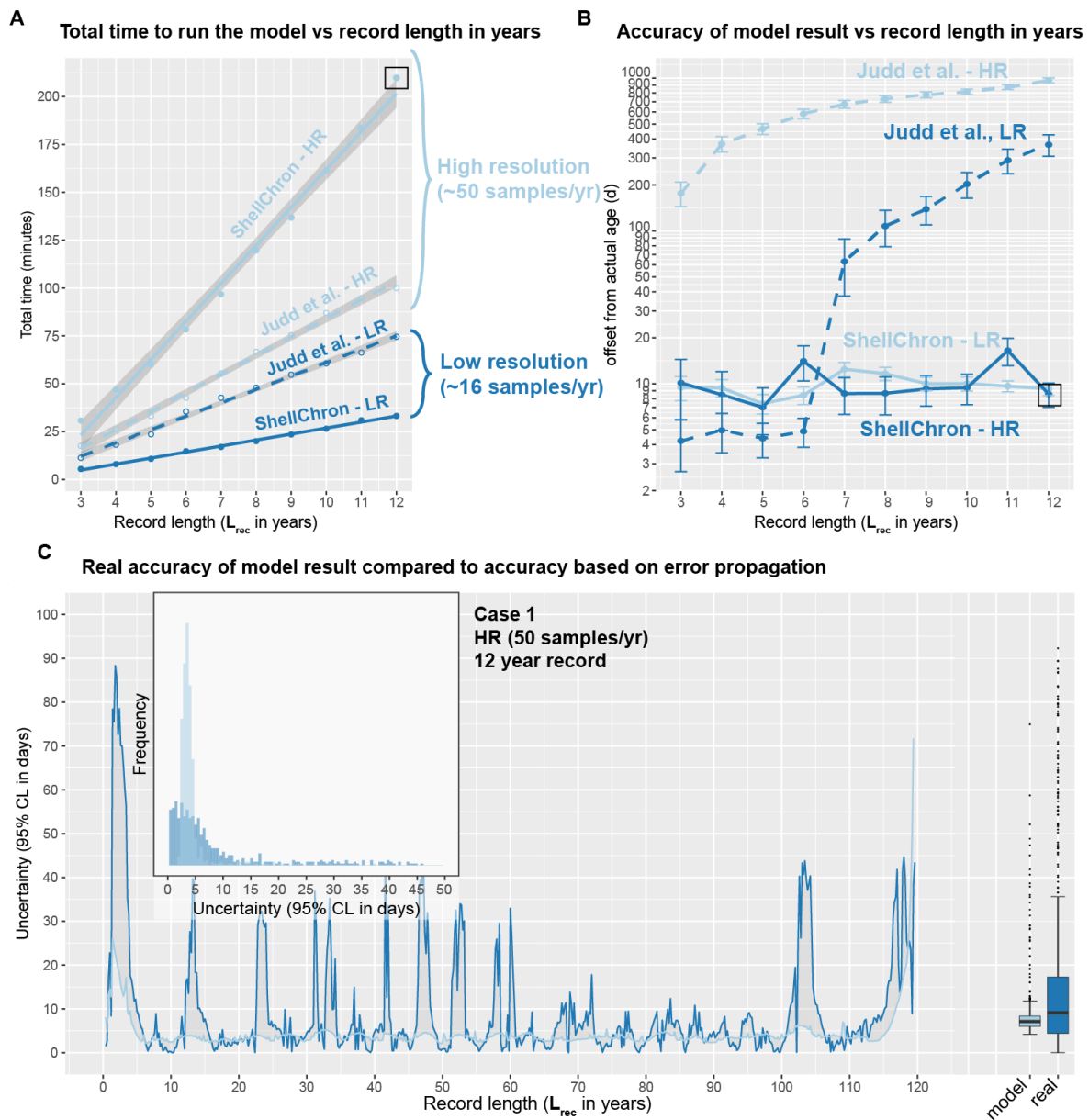
459

460 4.3 Natural carbonate records

461 Results of modelling natural carbonate records (**Fig. 7**; **Table 2**; see also **SI10**) illustrate the
462 effectiveness of ShellChron on different types of records. Performance clearly depends on the resolution
463 of the record and the regularity of seasonal variability contained within. As in the virtual datasets,
464 modelled $\delta^{18}\text{O}_c$ successfully mimic $\delta^{18}\text{O}_c$ data in all records ($\overline{\Delta^{18}\text{O}_c} = 0.0$; Spearman's ρ of 0.97, 0.91
465 and 0.92 for **coral**, **oyster** and **speleothem** respectively). No consistent seasonal bias is observed in
466 $\Delta^{18}\text{O}_c$ and model accuracy ($p > 0.05$; see **Table 2** and **SI12**), despite significant (seasonal and inter-
467 annual) variability contained in the records (especially in **oyster** and **speleothem** records). When
468 comparing the accuracy of these records, it must be noted that the “real” age of the samples in these
469 natural carbonates is not known. Model results are instead compared with age models constructed using
470 conventional techniques such as matching $\delta^{18}\text{O}_c$ profiles with local temperature and/or $\delta^{18}\text{O}_w$ variability
471 (**oyster** and **coral** records) or even merely by linear interpolation between annual markers in the record
472 (**speleothem** record; see **Supplementary Methods**). Despite this caveat, testing results clearly show
473 that the least complicated record (**coral**; **Fig. 7A**), characterized by minimal variability in $\delta^{18}\text{O}_w$ and
474 growth rate and a high sampling density, has the best overall model result ($\Delta^{18}\text{O}_c = 0.0 \pm 0.14$ compared
475 to a $\sim 1.7\text{‰}$ seasonal range; $\rho = 0.97$; $\Delta t = 12 \pm 28$ d; see **Table 2**). The **oyster** record (**Fig. 7B**), which
476 has strong seasonal variability in growth rate and $\delta^{18}\text{O}_{sw}$ also yields a very reliable age model ($\Delta^{18}\text{O}_c =$
477 0.0 ± 0.39 compared to a $\sim 3\text{‰}$ seasonal range; $\rho = 0.91$; $\Delta t = -15 \pm 43$ d; see **Table 2**). The **speleothem**
478 record (**Fig. 7C**), plagued by lower sampling resolution, large inter-annual $\delta^{18}\text{O}_c$ variability, restricted
479 $\delta^{18}\text{O}_c$ seasonality and a lack of clearly seasonal $\delta^{18}\text{O}_c$ forcing, yields the least reliable model result
480 ($\Delta^{18}\text{O}_c = 0.0 \pm 0.08$ compared to a $\sim 0.5\text{‰}$ seasonal range; $\rho = 0.92$; $\Delta t = -114 \pm 59$ d; see **Table 2**). Note
481 that the accuracy figure provided for the **speleothem** record is based on comparison with an age model
482 based on linear interpolation between annual growth lines. This assumption of the age-distance
483 relationship is almost certainly erroneous, since drip water supply to (and therefore growth in) has been
484 shown to vary seasonally (e.g. Baldini et al., 2008), including at the very site the **speleothem** data
485 derives from (Han-sur-Lesse cave, Belgium; Van Rampelbergh et al., 2014; Vansteenberge et al., 2019).
486 However, since no reliable information is available on sub-annual variability in growth rates in this record,
487 ShellChron results cannot be validated at the sub-annual scale in this case. The high age offset (-114
488 days) in the **speleothem** model result is a consequence of the assumption in ShellChron that the highest
489 temperature (lowest $\delta^{18}\text{O}_c$ value) recorded in each growth year happens halfway through the year (day

490 183). While this assumption is approximately valid for temperature-controlled $\delta^{18}\text{O}_c$ records (see **Fig. 6**
491 and **7**), it is problematic for speleothems, in which $\delta^{18}\text{O}_c$ is often dominated by the $\delta^{18}\text{O}_w$ of drip water,
492 which may not be lowest during the summer season (see Van Rampelbergh et al., 2014). The timing of
493 the $\delta^{18}\text{O}_c$ minimum can be set in the *run_model* function using the *t_maxtemp* parameter. Note that
494 changing *t_maxtemp* does not affect relative dating within the $\delta^{18}\text{O}_c$ record, but, if set correctly, results
495 in a phase shift of the age model result into better alignment with the seasonal cycle.

496



497

498 **Figure 8:** Overview of the result of timing ShellChron and the Judd et al. (2018) model on the same
 499 datasets **(A)**, comparing the accuracies of both models **(B)** and comparing the accuracy as calculated
 500 by ShellChron with the real offset in the age model **(C)**. In **(A)** and **(B)**, low resolution datasets are plotted
 501 in dark blue, while high-resolution datasets plot in light blue. Solid lines represent ShellChron and
 502 dashed lines show performance of the Judd et al. model. The black box in **(A)** and **(B)** highlights the
 503 dataset used in **(C)**. In **(C)**, dark blue lines, bars and boxplot indicate true offset of the model from the
 504 actual sample age, while light blue lines, bars and boxplot show the accuracy of the model as calculated
 505 from the propagated errors on model and input data. Raw data is provided in **SI11**.

506 4.4 Modeling time

507 The performance of both ShellChron and the Judd et al. model in terms of computation time linearly
508 increases with the length of the record (in years; see **Fig. 8**, **Fig. S5** and **SI11**). Computation time of
509 ShellChron on the high-resolution test dataset (50 samples/yr) increases very steeply with the length of
510 the record in years (~20 minutes per additional year), while the low-resolution dataset (16 samples/yr)
511 shows a slower increase (~3 minutes per additional year; **Fig. 5A**). This contrasts with the model from
512 Judd et al., which requires only slightly more time on high-resolution data than on low-resolution datasets
513 (~7 and ~10 minutes per additional year, respectively). The difference is explained by the sliding window
514 approach applied in ShellChron, which requires more SCEUA optimization runs per year in high-
515 resolution datasets than in low resolution datasets. When plotted against the number of calculation
516 windows or samples in the dataset, running ShellChron on low-resolution and high-resolution datasets
517 require a similar increase in computation time (~0.4 minutes, or 24 seconds, per additional
518 sample/window; **Fig. S5**) under default SCEUA conditions. ShellChron thus outcompetes the Judd et
519 al. model in terms of computation time in datasets with fewer than ~20 samples per year, even though
520 more SCEUA optimizations are required.

521 The key computational improvement in ShellChron is the application of a sinusoidal regression before
522 each SCEUA optimization to estimate the initial values of the modelled parameters (*sinreg* function; see
523 **equation 9** and **Fig. 1 in Model description**). Since carbonate archives are rarely sampled for stable
524 isotope measurements above 20 samples per year (e.g. Goodwin et al., 2003; Schöne et al., 2005;
525 Lough, 2010 and references therein), the disadvantage of a steep computational increase for very high-
526 resolution archives is, in practice, a favorable tradeoff for the added control on model and measurement
527 uncertainty and smoother inter-year transitions ShellChron offers in comparison to previous models.
528 The similarity of ShellChron's accuracy in the low- and high-resolution datasets demonstrates its
529 robustness across datasets with various sampling resolutions (see also **Table 2** and **Fig. 7**).

530 Longer computation times in the Judd et al. model result in slightly better accuracy on the modelled age
531 compared to ShellChron on the scale of individual datapoints in low-resolution datasets (see **Fig. 8B**).
532 However, this advantage is rapidly lost when records containing multiple years are considered (**Fig. 8B**).
533 The advantage of the ShellChron model is its application of overlapping model windows, which smooth
534 out the transitions between modelled years and eliminate accumulations of model inaccuracies when

535 records grow longer. In addition, contrary to previous models, ShellChron does not rely on user-defined
536 year boundaries, which may introduce mismatches between subsequent years to be propagated
537 through the age model, even in ideal datasets such as **Case 1 (Fig. 8B; see also Supplementary**
538 **Methods)**. By comparison, the overall accuracy of ShellChron is much more stable within and between
539 datasets of different length, while rarely introducing offsets of more than a month. More importantly,
540 where ShellChron takes into account the uncertainty on input parameters, this uncertainty is not
541 considered in most previous models (the MoGroFun model of Goodwin et al., 2003 being the exception).
542 The added uncertainty caused by input error is higher in less regular (sinusoidal) $\delta^{18}\text{O}_c$ records and in
543 records with lower sampling resolution, causing the uncertainties on the Judd et al., model reported here
544 for the ideal, high-resolution **Case 1** dataset to be over-optimistic. If ShellChron's model accuracy is
545 insufficient, its modular character allows the user to run the SCEUA algorithm to within more precise
546 optimization criteria by changing the model parameters (see **section 4.1**). However, this adaptation
547 comes at a cost of longer computation times.

548 The estimated uncertainty envelope (95% confidence interval) on the modelled age calculated by the
549 error propagation algorithm in ShellChron (4.7 ± 6.5 d) on average slightly underestimates the actual
550 offset between modelled age and real age in the **Case 1** record (9.3 ± 13.1 d; **Fig. 8C**). The foremost
551 difference between modelled and real uncertainty on the result is that the modelled uncertainty yields
552 a more smoothed record of uncertainty compared to the record of actual offset of the model (**Fig. 8C**).
553 ShellChron's uncertainty calculations are partly based on comparing overlapping model windows,
554 thereby smoothing out short term variations in model offset. The uncertainty of the model result (both
555 real and modelled) shows regular variability with a period of half a year (**Fig. 8C**). Comparing this
556 variability with the phase of the record (of which 6 years are plotted in **Fig. 6A**) reveals that the
557 uncertainty of the model is positively correlated to the slope of the $\delta^{18}\text{O}_c$ record. This is expected,
558 because in parts of the record with steep $\delta^{18}\text{O}_c$ -distance slopes, the local age model result is more
559 sensitive to small changes in the sampling distance, caused either by uncertainty in the model fit or
560 propagated uncertainty on the sampling distance defined by the user. The slight seasonal variability in
561 model accuracy in **Case 1** is also shown in **Fig. 6C** and comprises a difference in uncertainty of up to
562 10 days depending on the time of year in which the datapoint is found.

563 5. Applications and discussion

564 Its new features compared to previous age model routines make ShellChron a versatile package for
565 creating age models in a range of high-resolution paleoclimate records. The discussion above
566 demonstrates that ShellChron can reconstruct the age of individual $\delta^{18}\text{O}_c$ samples within monthly
567 precision. This level of precision is sufficient for accurate reconstructions of seasonality, defined as the
568 difference between warmest and coldest month (following USGS definitions; O'Donnell and Ignizio,
569 2012). While an improvement on this uncertainty could be of potential interest for ultra-high-resolution
570 paleoclimate studies (e.g. sub-daily variability, see Sano et al., 2012; Yan et al., 2020; de Winter et al.,
571 2020a), the increase in computation time and the sampling resolution such detailed age models demand
572 render age modelling from $\delta^{18}\text{O}_c$ records inefficient for this purpose (see **sections 4.1** and **4.4**). The
573 sampling resolution for high-resolution carbonate $\delta^{18}\text{O}_c$ records in the literature does not typically exceed
574 100 μm due to limitations in sampling acquisition (e.g. micromilling), which even in fast-growing archives
575 limits the resolution of these records to several days at best (see Gagan et al., 1994; Van Rangelbergh
576 et al., 2014; de Winter et al., 2020c). While in some archives, high-resolution ($< 100 \mu\text{m}$) trace element
577 records could be used to capture variability beyond this limit, the monthly age resolution of ShellChron
578 is sufficient for most typical high-resolution paleoclimate studies.

579 The ability to produce uninterrupted age models from multi-year records while considering both
580 variability in $\delta^{18}\text{O}_w$ and uncertainties on input parameters represent major advantages of ShellChron
581 over previous age modelling solutions. As a result, ShellChron can be applied on a wide range of
582 carbonate archives (see **Fig. 7** and **Table 2**). However, testing ShellChron on different records highlights
583 the limitations of the model inherited through its underlying assumptions. The most accurate model
584 results are obtained on records with minimal growth rate and $\delta^{18}\text{O}_w$ variability and a nearly sinusoidal
585 $\delta^{18}\text{O}_c$ record, such as tropical **coral** records (**Fig. 7A**; Gagan et al., 1994). In records where large
586 seasonal variability in growth rate and $\delta^{18}\text{O}_w$ does occur, such as in intertidal **oyster** shells, ShellChron's
587 accuracy slightly decreases, especially near growth hiatuses in the record (see **Fig. 7B**; Ullmann et al.,
588 2010). A worst-case scenario is represented by the **speleothem** record, which not only suffers from
589 much slower and more unpredictable growth rates and contains a comparatively small annual range in
590 $\delta^{18}\text{O}_c$, but it responds to $\delta^{18}\text{O}_w$ variability in drip water in the cave rather than temperature seasonality,
591 one of the assumptions underlying the current version of ShellChron (**Fig. 7C**; Vansteenberghe et al.,

592 2019). Despite these problems, ShellChron yields an age model that is remarkably accurate on an
593 annual timescale, which is as good as, or better than, the best age model that can be obtained by
594 applying layer counting on the most clearly laminated parts of the speleothem (e.g. Verheyden et al.,
595 2006). It must be noted that, while the close fit between modelled $\delta^{18}\text{O}_c$ and **speleothem** $\delta^{18}\text{O}_c$ data (ρ
596 = 0.92; σ = 0.08‰) is encouraging, a major reason for the model's success is the fact that the Proserpine
597 speleothem used in this example is known to receive significantly seasonal (though not sinusoidal) drip
598 water volumes and concentrations (Van Rampelbergh et al., 2014). Variability in drip water properties
599 and cave temperatures are known to differ strongly between cave systems (Fairchild et al., 2006;
600 Lachniet, 2009). For ShellChron (or any other $\delta^{18}\text{O}_c$ -based age model) to work reliably in speleothem
601 records, consistent seasonal variability in either temperature or $\delta^{18}\text{O}_w$ should be demonstrated to
602 significantly influence the $\delta^{18}\text{O}_c$ variability in the record. In practice, these constraints make ShellChron
603 applicable in speleothems for which the cave environment varies in response to the seasonal cycle,
604 such as localities overlain by thin epikarst, well-ventilated caves or speleothems situated close to the
605 cave entrance (Verheyden et al., 2006; Feng et al., 2013; Baker et al., 2021)

606 The difficulty of applying age model routines on speleothem records highlights one of the main
607 advantages of ShellChron over pre-existing age model routines, namely its modular character. Since
608 $\delta^{18}\text{O}_c$ records from some carbonate archives, such as speleothems, cannot be described by the
609 standard combination of temperature and growth rate sinusoids on which ShellChron is based (in its
610 current version), the possibility to adapt the “building block” functions used to approximate these $\delta^{18}\text{O}_c$
611 records (*d18O_model*, *temperature_curve* and *growth_rate_curve*; see **Fig. 1**) while leaving the core
612 structure of ShellChron intact greatly augments the versatility of the model. The freedom to adapt the
613 building blocks used to approximate the $\delta^{18}\text{O}_c$ record theoretically enables ShellChron to model sub-
614 annual age-distance relationships in any record as long as the seasonal variability in the variables used
615 to model the input data are predictable and can be represented by a function. For example, since
616 speleothem $\delta^{18}\text{O}_c$ records often depend on variability in the $\delta^{18}\text{O}_w$ value of the drip water, a function
617 describing this variability through the year can replace the *temperature_curve* function to create more
618 accurate sub-annual age models for speleothems (e.g. Matthey et al., 2008; Lachniet, 2009; Van
619 Rampelbergh et al., 2014). Similarly, the *growth_rate_curve* function can be modified in case the default
620 skewed sinusoid does not accurately describe the extension rate of the record under study, and the
621 *d18O_model* function can be adapted to feature the most fitting $\delta^{18}\text{O}_c$ -temperature or $\delta^{18}\text{O}_c$ - $\delta^{18}\text{O}_w$

622 relationship. Note that the flexibility of this approach is limited by the expression of the annual cycle in
623 the $\delta^{18}\text{O}_c$ record. The $\delta^{18}\text{O}_c$ -based dating approach in ShellChron will therefore have severe trouble
624 dating records in which the annual $\delta^{18}\text{O}_c$ variability is severely dampened, such as speleothems in
625 deeper cave systems (e.g. Vansteenberge et al., 2016), or in which annual $\delta^{18}\text{O}_c$ variability is not
626 sinusoidal, such as tropical records with bimodal temperature or precipitation seasonality (Knoben et
627 al., 2018).

628 Flexibility in the definition of “building block” functions used to approximate the input data paves the way
629 for future application beyond carbonate $\delta^{18}\text{O}_c$ records. The seasonal variability in $\delta^{18}\text{O}$ in some ice cores
630 can be approximated by a stable and unbiased temperature relationship (van Ommen and Morgan,
631 1997). ShellChron can therefore be modified to date sub-annual samples in these ice core records and
632 reconstruct seasonal variability in the high latitudes through the Quarternary. Similarly, inter-annual $\delta^{18}\text{O}$
633 variability in tree ring records are demonstrated to record variability in precipitation through the year,
634 and this variability can be modelled to improve sub-annual age models in these records (Xu et al., 2016).
635 More generally, the field of dendrochemistry has recently developed additional chemical proxies for
636 seasonality (e.g. trace element concentrations), which can be measured on smaller sample volumes
637 (and thus greater resolution) to obtain ultra-high-resolution records on which (sub-annual) dating can be
638 based (e.g. Poussart et al., 2006; Superville et al., 2017). A similar development has taken place in the
639 study of carbonate bio-archives such as corals and mollusks, of which some show strong, predictable
640 seasonal variability in trace elements (e.g. Mg/Ca and Sr/Ca ratios) which can be used to accurately
641 date these records (de Villiers et al., 1995; Sosdian et al., 2006; Durham et al., 2017). Minor changes in
642 the “building block” functions using empirical transfer functions for these trace element records will
643 enable ShellChron to capitalize on these relationships and reconstruct sub-annual growth rates with
644 improved precision due to the higher precision with which these proxies can be measured compared to
645 $\delta^{18}\text{O}_c$ records. Finally, the application of ShellChron for age model construction is not necessarily limited
646 to the seasonal cycle, as other major cycles in climate (e.g. tidal, diurnal or Milankovitch cycles) leave
647 similar marks on climate records and can thus be used as basis for age modelling (e.g. Sano et al.,
648 2012; Huyghe et al., 2019; de Winter et al., 2020a; Sinnesael et al., 2020). It must be noted that, since
649 ShellChron was developed for modeling based on annual periodicity, applying it on other timescales
650 would require more thorough adaptation of the model code than merely adapting the “building block”
651 functions to support additional proxy systems.

652 While age reconstructions are the main aim of ShellChron, the model also yields information about the
653 temperature and growth rate parameters used in each simulation window to approximate the local $\delta^{18}\text{O}_c$
654 curve (see *parameter matrix* in **Fig. 1** and **SI6**). These parameters hold key information about the
655 response of the archive to seasonal changes in the environment, such as the season of growth,
656 relationships between growth rate and temperature and the temperature range that is recorded.
657 Combining these parameters with records of influential environmental variables such as seawater
658 chlorophyll concentration or local precipitation patterns yields information about the response of the
659 climate archive to environmental variables, in addition to the climate or environmental change it records.
660 Study examples include the relationship between growth rate of marine calcifiers and phytoplankton
661 abundance or the correlation between precipitation patterns and chemical variability in speleothems.
662 While such discussion is beyond the scope of this work, examples of parameter distributions are
663 provided in **SI5**, and the application of modelled growth rate parameters in bivalve sclerochronology is
664 discussed in more detail in Judd et al. (2018). Note that the sliding window approach of ShellChron
665 produces records of changing temperature and growth rate parameters at the scale of individual
666 samples (albeit smoothed by the sliding window approach) rather than annually, as in Judd et al. (2018).

667

668 **6. Conclusions**

669 ShellChron offers a novel, open-source solution to the problem of dating carbonate archives for high-
670 resolution paleoclimate reconstruction on a sub-annual scale. Based on critical evaluation of previous
671 age models, building on their strengths while attempting to eliminate their weaknesses, ShellChron
672 provides continuous age models based on $\delta^{18}\text{O}_c$ -profiles in these archives with monthly accuracy,
673 considering the uncertainties associated with both the model itself and the input data. The monthly
674 accuracy of the model, as tested on a range of virtual and natural datasets, enables its application for
675 age determination in studies of seasonal climate and environmental variability. Higher accuracies can
676 be reached at the cost of longer computation times by adapting the model parameters, but age
677 determinations far beyond the monthly scale are unlikely to be feasible considering the limitations on
678 sampling resolution and measurement uncertainties on $\delta^{18}\text{O}_c$ records. ShellChron's computation times
679 on datasets with sampling resolutions typical for the paleoclimatology field (up to 20 samples/yr) remain
680 practical and comparable to previous model solutions, despite adding several features that improve the

681 versatility and interpretation of model results. Its modular design allows ShellChron to be adapted to
682 different situations with comparative ease. It thereby functions as a platform for age-distance modelling
683 on a wide range of climate and environmental archives and is not limited in its application to the $\delta^{18}\text{O}_c$
684 proxy, the carbonate substrate or even to the annual cycle, as long as the relationship between the
685 proxy and the extension rate of the archive on a given time scale can be parameterized. Future
686 improvements will capitalize on this variability, expanding ShellChron beyond its current dependency on
687 the $\delta^{18}\text{O}_c$ -temperature relationship in carbonates. Members of the high-resolution paleoclimate
688 community are invited to contribute to this effort by adapting the model for their purpose.

689

690 **Code availability**

691 ShellChron is worked out into a fully functioning package for the open-source computational language
692 R (version 3.5.0 or later; R Core Team, 2020). The most recent full version (v0.4.0) of the ShellChron
693 passed the code review of the Comprehensive R Archive Network (CRAN) and is freely available for
694 download as an R package on the CRAN server (see <https://CRAN.R-project.org/package=ShellChron>).
695 The CRAN server entry also includes detailed line-by-line documentation of the code and working
696 examples for every function. In addition, the latest development version of ShellChron is available on
697 GitHub (<https://github.com/nielsjdewinter/ShellChron>). Those interested in adapting ShellChron for their
698 research purposes are invited to do so here. Code and documentation, together with all supplementary
699 files belonging to this study, are also available on the open-source online repository Zenodo
700 (<http://doi.org/10.5281/zenodo.4288344>).

701

702 **Author contribution**

703 NJW designed the study, wrote the model script, carried out the test calculations and wrote the
704 manuscript.

705

706 **Competing interests**

707 There were no competing interests to declare.

708

709 **Acknowledgements**

710 This research project is part of the UNBIAS project funded by the European Commission through a
711 Marie Curie Individual Fellowship (MSCA-IF; grant number: 843011) and the Flemish Research Council
712 (FWO; junior postdoc grant, project number: 12ZB220N). Thanks go to Emily Judd for discussions about
713 the workings of the Judd et al. (2018) model and its potential adaptation beyond aragonitic mollusk
714 shells. High-resolution temperature and salinity data from the NIOZ jetty which underlie the **Texel**
715 dataset and the noise added to the idealized **Case 1** dataset were kindly provided by Eric Wagemakers
716 and Sonja van Leeuwen (Royal Dutch Institute for Sea Research, the Netherlands). The $\delta^{18}\text{O}_c$ data
717 series from the *Crassostrea gigas* (**oyster**) and Proserpine stalagmite (**speleothem**) were generously
718 provided by dr. Clemens V. Ullmann (University of Exeter, UK) and dr. Stef Vansteenberge (Vrije
719 Universiteit Brussel, Belgium), respectively. Raw data from the *Porites lutea* **coral** dataset were obtained
720 with help of the WebPlotDigitizer (<https://automeris.io/WebPlotDigitizer/>) developed by Ankit Rohatgi.
721 Preparation of the ShellChron model into an R package would not have been possible without the helpful
722 instructions by Fong Chun Chan ([https://tinyheero.github.io/jekyll/update/2015/07/26/making-your-first-](https://tinyheero.github.io/jekyll/update/2015/07/26/making-your-first-R-package.html)
723 [R-package.html](https://tinyheero.github.io/jekyll/update/2015/07/26/making-your-first-R-package.html)), Hilary Parker ([https://hilaryparker.com/2014/04/29/writing-an-r-package-from-](https://hilaryparker.com/2014/04/29/writing-an-r-package-from-scratch/)
724 [scratch/](https://hilaryparker.com/2014/04/29/writing-an-r-package-from-scratch/)) and Hadley Wickham (<https://r-pkgs.org/release.html>) as well as the insightful and inspiring
725 discussions on R coding and statistics with Ilja Kocken (Utrecht University). In addition, distribution of
726 the code in an organized way was made possible thanks to Git (<https://git-scm.com/>) and Github
727 (<https://github.com/>) and the R Project Team (<https://www.r-project.org/>), with special thanks to Uwe
728 Ligges (University of Dortmund, Germany) and Gregor Seyer (University of Vienna, Austria) for their
729 comments on initial submissions of the package to the CRAN database. Thanks go to William A. Huber
730 (<https://www.analysisandinference.com/team/william-a-huber-phd>) for providing a practical general
731 solution to the peak identification problem in the *cumulative_day* function (see *peakid* function and
732 https://rpubs.com/mengxu/peak_detection).

733

734 **References**

- 735 Bajnai D., Guo W., Spötl C., Coplen T. B., Methner K., Löffler N., Krsnik E., Gischler E., Hansen M.,
 736 Henkel D., Price G. D., Raddatz J., Scholz D. and Fiebig J. (2020) Dual clumped isotope thermometry
 737 resolves kinetic biases in carbonate formation temperatures. *Nature Communications* **11**, 4005.
- 738 Baker A., Mariethoz G., Comas-Bru L., Hartmann A., Frisia S., Borsato A., Treble P. C. and Asrat A.
 739 (2021) The Properties of Annually Laminated Stalagmites-A Global Synthesis. *Reviews of Geophysics*
 740 **59**, e2020RG000722.
- 741 Baldini J. U. L., McDermott F., Hoffmann D. L., Richards D. A. and Clipson N. (2008) Very high-
 742 frequency and seasonal cave atmosphere PCO₂ variability: Implications for stalagmite growth and
 743 oxygen isotope-based paleoclimate records. *Earth and Planetary Science Letters* **272**, 118–129.
- 744 Brand W. A., Coplen T. B., Vogl J., Rosner M. and Prohaska T. (2014) Assessment of international
 745 reference materials for isotope-ratio analysis (IUPAC Technical Report). *Pure and Applied Chemistry*
 746 **86**, 425–467.
- 747 de Brauwere A., De Ridder F., Pintelon R., Schoukens J. and Dehairs F. (2009) A comparative study
 748 of methods to reconstruct a periodic time series from an environmental proxy record. *Earth-Science*
 749 *Reviews* **95**, 97–118.
- 750 Butler P. G., Wanamaker A. D., Scourse J. D., Richardson C. A. and Reynolds D. J. (2013) Variability
 751 of marine climate on the North Icelandic Shelf in a 1357-year proxy archive based on growth
 752 increments in the bivalve *Arctica islandica*. *Palaeogeography, Palaeoclimatology, Palaeoecology* **373**,
 753 141–151.
- 754 Chauvaud L., Lorrain A., Dunbar R. B., Paulet Y.-M., Thouzeau G., Jean F., Guarini J.-M. and
 755 Mucciarone D. (2005) Shell of the Great Scallop *Pecten maximus* as a high-frequency archive of
 756 paleoenvironmental changes. *Geochemistry, Geophysics, Geosystems* **6**.
- 757 Coplen T. B. (2007) Calibration of the calcite–water oxygen-isotope geothermometer at Devils Hole,
 758 Nevada, a natural laboratory. *Geochimica et Cosmochimica Acta* **71**, 3948–3957.
- 759 Daëron M., Drysdale R. N., Peral M., Huyghe D., Blamart D., Coplen T. B., Lartaud F. and Zanchetta
 760 G. (2019) Most Earth-surface calcites precipitate out of isotopic equilibrium. *Nature Communications*
 761 **10**, 429.
- 762 Daëron M., Guo W., Eiler J., Genty D., Blamart D., Boch R., Drysdale R., Maire R., Wainer K. and
 763 Zanchetta G. (2011) ¹³C/¹⁸O clumping in speleothems: Observations from natural caves and
 764 precipitation experiments. *Geochimica et Cosmochimica Acta* **75**, 3303–3317.
- 765 De Ridder F., de Brauwere A., Pintelon R., Schoukens J., Dehairs F., Baeyens W. and Wilkinson B. H.
 766 (2007) Comment on: Paleoclimatic inference from stable isotope profiles of accretionary biogenic
 767 hardparts—a quantitative approach to the evaluation of incomplete data, by Wilkinson, BH, Ivany, LC,
 768 2002. *Palaeogeogr. Palaeocl. Palaeoecol.* **185**, 95–114. *Palaeogeography, Palaeoclimatology,*
 769 *Palaeoecology* **248**, 473–476.
- 770 DeCarlo T. M. and Cohen A. L. (2017) Dissepiments, density bands and signatures of thermal stress
 771 in *Porites* skeletons. *Coral Reefs* **36**, 749–761.
- 772 Dettman D. L., Reische A. K. and Lohmann K. C. (1999) Controls on the stable isotope composition of
 773 seasonal growth bands in aragonitic fresh-water bivalves (Unionidae). *Geochimica et Cosmochimica*
 774 *Acta* **63**, 1049–1057.
- 775 Duan Q., Sorooshian S. and Gupta V. (1992) Effective and efficient global optimization for conceptual
 776 rainfall-runoff models. *Water resources research* **28**, 1015–1031.
- 777 Dunbar R. B. and Wellington G. M. (1981) Stable isotopes in a branching coral monitor seasonal
 778 temperature variation. *Nature* **293**, 453–455.
- 779 Durham S. R., Gillikin D. P., Goodwin D. H. and Dietl G. P. (2017) Rapid determination of oyster
 780 lifespans and growth rates using LA-ICP-MS line scans of shell Mg/Ca ratios. *Palaeogeography,*
 781 *Palaeoclimatology, Palaeoecology.*

- 782 Epstein S., Buchsbaum R., Lowenstam H. A. and Urey H. C. (1953) Revised carbonate-water isotopic
783 temperature scale. *Geological Society of America Bulletin* **64**, 1315–1326.
- 784 Evans M. N. and Schrag D. P. (2004) A stable isotope-based approach to tropical dendroclimatology
785 Associate editor: D. W. Lea. *Geochimica et Cosmochimica Acta* **68**, 3295–3305.
- 786 Fairchild I. J., Smith C. L., Baker A., Fuller L., Spötl C., Matthey D., McDermott F., and others (2006)
787 Modification and preservation of environmental signals in speleothems. *Earth-Science Reviews* **75**,
788 105–153.
- 789 Feng W., Casteel R. C., Banner J. L. and Heinze-Fry A. (2014) Oxygen isotope variations in rainfall,
790 drip-water and speleothem calcite from a well-ventilated cave in Texas, USA: Assessing a new
791 speleothem temperature proxy. *Geochimica et Cosmochimica Acta* **127**, 233–250.
- 792 Frisia S., Borsato A., Fairchild I. J. and McDermott F. (2000) Calcite fabrics, growth mechanisms, and
793 environments of formation in speleothems from the Italian Alps and southwestern Ireland. *Journal of*
794 *Sedimentary Research* **70**, 1183–1196.
- 795 Gagan M. K., Chivas A. R. and Isdale P. J. (1994) High-resolution isotopic records from corals using
796 ocean temperature and mass-spawning chronometers. *Earth and Planetary Science Letters* **121**, 549–
797 558.
- 798 Goodwin D. H., Paul P. and Wissink C. L. (2009) MoGroFunGen: A numerical model for reconstructing
799 intra-annual growth rates of bivalve molluscs. *Palaeogeography, Palaeoclimatology, Palaeoecology*
800 **276**, 47–55.
- 801 Goodwin D. H., Schöne B. R. and Dettman D. L. (2003) Resolution and Fidelity of Oxygen Isotopes as
802 Paleotemperature Proxies in Bivalve Mollusk Shells: Models and Observations. *PALAIOS* **18**, 110–
803 125.
- 804 Grossman E. L. and Ku T.-L. (1986) Oxygen and carbon isotope fractionation in biogenic aragonite:
805 temperature effects. *Chemical Geology: Isotope Geoscience section* **59**, 59–74.
- 806 Huybers P. and Curry W. (2006) Links between annual, Milankovitch and continuum temperature
807 variability. *Nature* **441**, 329.
- 808 Huyghe D., de Rafelis M., Ropert M., Mouchi V., Emmanuel L., Renard M. and Lartaud F. (2019) New
809 insights into oyster high-resolution hinge growth patterns. *Mar Biol* **166**, 48.
- 810 IPCC (2018) *GLOBAL WARMING OF 1.5 °C an IPCC special report on the impacts of global warming*
811 *of 1.5 °C above pre-industrial levels and related global greenhouse gas emission pathways, in the*
812 *context of strengthening the global response to the threat of climate change, sustainable development,*
813 *and efforts to eradicate poverty.*
- 814 Ivany L. C. and Runnegar B. (2010) Early Permian seasonality from bivalve $\delta^{18}\text{O}$ and implications for
815 the oxygen isotopic composition of seawater. *Geology* **38**, 1027–1030.
- 816 Jones D. S. (1983) Sclerochronology: Reading the Record of the Molluscan Shell: Annual growth
817 increments in the shells of bivalve molluscs record marine climatic changes and reveal surprising
818 longevity. *American Scientist* **71**, 384–391.
- 819 Jones D. S. and Quitmyer I. R. (1996) Marking Time with Bivalve Shells: Oxygen Isotopes and Season
820 of Annual Increment Formation. *PALAIOS* **11**, 340–346.
- 821 Judd E. J., Wilkinson B. H. and Ivany L. C. (2018) The life and time of clams: Derivation of intra-annual
822 growth rates from high-resolution oxygen isotope profiles. *Palaeogeography, Palaeoclimatology,*
823 *Palaeoecology* **490**, 70–83.
- 824 Kim S.-T. and O'Neil J. R. (1997) Equilibrium and nonequilibrium oxygen isotope effects in synthetic
825 carbonates. *Geochimica et Cosmochimica Acta* **61**, 3461–3475.
- 826 Knoben W. J. M., Woods R. A. and Freer J. E. (2019) Global bimodal precipitation seasonality: A
827 systematic overview. *International Journal of Climatology* **39**, 558–567.
- 828 Lachniet M. S. (2009) Climatic and environmental controls on speleothem oxygen-isotope values.
829 *Quaternary Science Reviews* **28**, 412–432.

- 830 Le Tissier M. D. A., Clayton B., Brown B. E. and Davis P. S. (1994) Skeletal correlates of coral density
831 banding and an evaluation of radiography as used in sclerochronology. *Marine Ecology Progress*
832 *Series* **110**, 29–44.
- 833 LeGrande A. N. and Schmidt G. A. (2006) Global gridded data set of the oxygen isotopic composition
834 in seawater. *Geophysical research letters* **33**.
- 835 Lough J. M. (2010) Climate records from corals. *WIREs Climate Change* **1**, 318–331.
- 836 Mahé K., Bellamy E., Lartaud F. and Rafélis M. de (2010) Calcein and manganese experiments for
837 marking the shell of the common cockle (*Cerastoderma edule*): tidal rhythm validation of increments
838 formation. *Aquat. Living Resour.* **23**, 239–245.
- 839 Matthey D., Lowry D., Duffet J., Fisher R., Hodge E. and Frisia S. (2008) A 53 year seasonally resolved
840 oxygen and carbon isotope record from a modern Gibraltar speleothem: Reconstructed drip water and
841 relationship to local precipitation. *Earth and Planetary Science Letters* **269**, 80–95.
- 842 McCrea J. M. (1950) On the Isotopic Chemistry of Carbonates and a Paleotemperature Scale. *J.*
843 *Chem. Phys.* **18**, 849–857.
- 844 Mitchell Jr. J. M. (1976) An overview of climatic variability and its causal mechanisms. *Quaternary*
845 *Research* **6**, 481–493.
- 846 Mohr R. C., Tobin T. S., Petersen S. V., Dutton A. and Oliphant E. (2020) Subannual stable isotope
847 records reveal climate warming and seasonal anoxia associated with two extinction intervals across
848 the Cretaceous-Paleogene boundary on Seymour Island, Antarctica. *Geology* **48**, 1131–1136.
- 849 Müller P., Taylor M. H., Klicpera A., Wu H. C., Michel J. and Westphal H. (2015) Food for thought:
850 Mathematical approaches for the conversion of high-resolution sclerochronological oxygen isotope
851 records into sub-annually resolved time series. *Palaeogeography, Palaeoclimatology, Palaeoecology*
852 **440**, 763–776.
- 853 O'Donnell M. S. and Ignizio D. A. (2012) Bioclimatic predictors for supporting ecological applications in
854 the conterminous United States. *US Geological Survey Data Series* **691**.
- 855 Ommen T. D. van and Morgan V. (1997) Calibrating the ice core paleothermometer using seasonality.
856 *Journal of Geophysical Research: Atmospheres* **102**, 9351–9357.
- 857 Poussart P. M., Myneni S. C. B. and Lanzirotti A. (2006) Tropical dendrochemistry: A novel approach
858 to estimate age and growth from ringless trees. *Geophysical Research Letters* **33**.
- 859 R Core Team (2020) *R: A Language and Environment for Statistical Computing.*, R Foundation for
860 Statistical Computing, Vienna, Austria.
- 861 Rohling E. J. (2013) Oxygen isotope composition of seawater. *The Encyclopedia of Quaternary*
862 *Science. Amsterdam: Elsevier* **2**, 915–922.
- 863 Saenger C., Gabitov R. I., Farmer J., Watkins J. M. and Stone R. (2017) Linear correlations in bamboo
864 coral $\delta^{13}\text{C}$ and $\delta^{18}\text{O}$ sampled by SIMS and micromill: Evaluating paleoceanographic potential and
865 biomineralization mechanisms using $\delta^{11}\text{B}$ and $\Delta 47$ composition. *Chemical Geology* **454**, 1–14.
- 866 Sano Y., Kobayashi S., Shirai K., Takahata N., Matsumoto K., Watanabe T., Sowa K. and Iwai K.
867 (2012) Past daily light cycle recorded in the strontium/calcium ratios of giant clam shells. *Nature*
868 *Communications* **3**, 761.
- 869 Schöne B. R., Fiebig J., Pfeiffer M., Gleß R., Hickson J., Johnson A. L., Dreyer W. and Oschmann W.
870 (2005) Climate records from a bivalved Methuselah (*Arctica islandica*, Mollusca; Iceland).
871 *Palaeogeography, Palaeoclimatology, Palaeoecology* **228**, 130–148.
- 872 Schöne B. R. and Gillikin D. P. (2013) Unraveling environmental histories from skeletal diaries —
873 Advances in sclerochronology. *Palaeogeography, Palaeoclimatology, Palaeoecology* **373**, 1–5.
- 874 Schöne B. R., Zhang Z., Radermacher P., Thébault J., Jacob D. E., Nunn E. V. and Maurer A.-F.
875 (2011) Sr/Ca and Mg/Ca ratios of ontogenetically old, long-lived bivalve shells (*Arctica islandica*) and
876 their function as paleotemperature proxies. *Palaeogeography, Palaeoclimatology, Palaeoecology* **302**,
877 52–64.

- 878 Sinnesael M., De Vleeschouwer D., Zeeden C., Batenburg S. J., Da Silva A.-C., de Winter N. J.,
879 Dinarès-Turell J., Drury A. J., Gambacorta G. and Hilgen F. J. (2019) The Cyclostratigraphy
880 Intercomparison Project (CIP): consistency, merits and pitfalls. *Earth-Science Reviews*, 102965.
- 881 Sosdian S., Gentry D. K., Lear C. H., Grossman E. L., Hicks D. and Rosenthal Y. (2006) Strontium to
882 calcium ratios in the marine gastropod *Conus ermineus*: Growth rate effects and temperature
883 calibration. *Geochemistry, Geophysics, Geosystems* **7**.
- 884 Steuber T., Rauch M., Masse J.-P., Graaf J. and Malkoč M. (2005) Low-latitude seasonality of
885 Cretaceous temperatures in warm and cold episodes. *Nature* **437**, 1341–1344.
- 886 Superville P.-J., De Winter N., Phung A. T., Proix N., Baeyens W. and Gao Y. (2017) Radial metal
887 concentration profiles in trees growing on highly contaminated soils. *Chemosphere* **172**, 80–88.
- 888 Tarutani T., Clayton R. N. and Mayeda T. K. (1969) The effect of polymorphism and magnesium
889 substitution on oxygen isotope fractionation between calcium carbonate and water. *Geochimica et*
890 *Cosmochimica Acta* **33**, 987–996.
- 891 Treble P. C., Schmitt A. K., Edwards R. L., McKeegan K. D., Harrison T. M., Grove M., Cheng H. and
892 Wang Y. J. (2007) High resolution Secondary Ionisation Mass Spectrometry (SIMS) $\delta^{18}\text{O}$ analyses of
893 Hulu Cave speleothem at the time of Heinrich Event 1. *Chemical Geology* **238**, 197–212.
- 894 Ullmann C. V., Böhm F., Rickaby R. E., Wiechert U. and Korte C. (2013) The Giant Pacific Oyster
895 (*Crassostrea gigas*) as a modern analog for fossil ostreoids: isotopic (Ca, O, C) and elemental (Mg/Ca,
896 Sr/Ca, Mn/Ca) proxies. *Geochemistry, Geophysics, Geosystems* **14**, 4109–4120.
- 897 Ullmann C. V. and Korte C. (2015) Diagenetic alteration in low-Mg calcite from macrofossils: a review.
898 *Geological Quarterly* **59**, 3–20.
- 899 Ullmann C. V., Wiechert U. and Korte C. (2010) Oxygen isotope fluctuations in a modern North Sea
900 oyster (*Crassostrea gigas*) compared with annual variations in seawater temperature: Implications for
901 palaeoclimate studies. *Chemical Geology* **277**, 160–166.
- 902 Urban F. E., Cole J. E. and Overpeck J. T. (2000) Influence of mean climate change on climate
903 variability from a 155-year tropical Pacific coral record. *Nature* **407**, 989–993.
- 904 Urey H. C. (1948) Oxygen Isotopes in Nature and in the Laboratory. *Science* **108**, 489–496.
- 905 Van Rampelbergh M., Verheyden S., Allan M., Quinif Y., Keppens E. and Claeys P. (2014) Seasonal
906 variations recorded in cave monitoring results and a 10 year monthly resolved speleothem $\delta^{18}\text{O}$ and
907 $\delta^{13}\text{C}$ record from the Han-sur-Lesse cave, Belgium. *Climate of the Past Discussions* **10**, 1821–1856.
- 908 Vansteenberge S., Verheyden S., Cheng H., Edwards R. L., Keppens E. and Claeys P. (2016)
909 Paleoclimate in continental northwestern Europe during the Eemian and early Weichselian (125–
910 97 ka): insights from a Belgian speleothem. *Clim. Past* **12**, 1445–1458.
- 911 Vansteenberge S., Winter N. de, Sinnesael M., Verheyden S., Goderis S., Malderen S. J. M. V.,
912 Vanhaecke F. and Claeys P. (2019) Reconstructing seasonality through stable isotope and trace
913 element analysis of the Proserpine stalagmite, Han-sur-Lesse Cave, Belgium: indications for climate-
914 driven changes during the last 400 years. *Climate of the Past Discussions*, 1–32.
- 915 Verheyden S., Baele J.-M., Keppens E., Genty D., Cattani O., Cheng H., LAWRENCE E., ZHANG H.,
916 Van Strijdonck M. and Quinif Y. (2006) The Proserpine stalagmite (Han-Sur-Lesse Cave, Belgium):
917 preliminary environmental interpretation of the last 1000 years as recorded in a layered speleothem.
918 *Geologica Belgica*.
- 919 de Villiers S., Nelson B. K. and Chivas A. R. (1995) Biological controls on coral Sr/Ca and $\delta^{18}\text{O}$
920 reconstructions of sea surface temperatures. *Science* **269**, 1247.
- 921 Wang Y. J., Cheng H., Edwards R. L., An Z. S., Wu J. Y., Shen C.-C. and Dorale J. A. (2001) A High-
922 Resolution Absolute-Dated Late Pleistocene Monsoon Record from Hulu Cave, China. *Science* **294**,
923 2345–2348.
- 924 Watkins J. M., Hunt J. D., Ryerson F. J. and DePaolo D. J. (2014) The influence of temperature, pH,
925 and growth rate on the $\delta^{18}\text{O}$ composition of inorganically precipitated calcite. *Earth and Planetary*
926 *Science Letters* **404**, 332–343.

- 927 Wilkinson B. H. and Ivany L. C. (2002) Paleoclimatic inference from stable isotope profiles of
928 accretionary biogenic hardparts – a quantitative approach to the evaluation of incomplete data.
929 *Palaeogeography, Palaeoclimatology, Palaeoecology* **185**, 95–114.
- 930 de Winter N., Vellekoop J., Vorsselmans R., Golreihan A., Soete J., Petersen S., Meyer K., Casadio
931 S., Speijer R. and Claeys P. (2018) An assessment of latest Cretaceous Pycnodonte vesicularis
932 (Lamarck, 1806) shells as records for palaeoseasonality: a multi-proxy investigation. *Climate of the*
933 *Past* **14**, 725–749.
- 934 de Winter N. J., Agterhuis T. and Ziegler M. (2021) Optimizing sampling strategies in high-resolution
935 paleoclimate records. *Climate of the Past* **17**, 1315–1340.
- 936 de Winter N. J., Goderis S., Dehairs F., Jagt J. W., Fraaije R. H., Van Malderen S. J., Vanhaecke F.
937 and Claeys P. (2017) Tropical seasonality in the late Campanian (late Cretaceous): Comparison
938 between multiproxy records from three bivalve taxa from Oman. *Palaeogeography, Palaeoclimatology,*
939 *Palaeoecology* **485**, 740–760.
- 940 de Winter N. J., Goderis S., Malderen S. J. M. V., Sinnesael M., Vansteenberge S., Snoeck C., Belza
941 J., Vanhaecke F. and Claeys P. (2020a) Subdaily-Scale Chemical Variability in a *Torreites Sanchezi*
942 Rudist Shell: Implications for Rudist Paleobiology and the Cretaceous Day-Night Cycle.
943 *Paleoceanography and Paleoclimatology* **35**, e2019PA003723.
- 944 de Winter N. J., Ullmann C. V., Sørensen A. M., Thibault N., Goderis S., Van Malderen S. J. M.,
945 Snoeck C., Goolaerts S., Vanhaecke F. and Claeys P. (2020b) Shell chemistry of the boreal
946 Campanian bivalve *Rastellum diluvianum* (Linnaeus, 1767) reveals temperature
947 seasonality, growth rates and life cycle of an extinct Cretaceous oyster. *Biogeosciences* **17**, 2897–
948 2922.
- 949 de Winter N. J., Vellekoop J., Clark A. J., Stassen P., Speijer R. P. and Claeys P. (2020c) The giant
950 marine gastropod *Campanile giganteum* (Lamarck, 1804) as a high-resolution archive of seasonality in
951 the Eocene greenhouse world. *Geochemistry, Geophysics, Geosystems* **21**, e2019GC008794.
- 952 Xu C., Zheng H., Nakatsuka T., Sano M., Li Z. and Ge J. (2016) Inter-and intra-annual tree-ring
953 cellulose oxygen isotope variability in response to precipitation in Southeast China. *Trees* **30**, 785–
954 794.
- 955 Yan H., Liu C., An Z., Yang W., Yang Yuanjian, Huang P., Qiu S., Zhou P., Zhao N., Fei H., Ma X., Shi
956 G., Dodson J., Hao J., Yu K., Wei G., Yang Yanan, Jin Z. and Zhou W. (2020) Extreme weather
957 events recorded by daily to hourly resolution biogeochemical proxies of marine giant clam shells.
958 *PNAS* **117**, 7038–7043.
- 959 Zhu F., Emile-Geay J., McKay N. P., Hakim G. J., Khider D., Ault T. R., Steig E. J., Dee S. and
960 Kirchner J. W. (2019) Climate models can correctly simulate the continuum of global-average
961 temperature variability. *PNAS* **116**, 8728–8733.
962